Monthly Notices
of the
ROYAL ASTRONOMICAL SOCIETY

MNRAS **484,** 4865–4880 (2019)
Advance Access publication 2019 February 1

doi:10.1093/mnras/stz326

Halo mass estimates from the globular cluster populations of 175 low surface brightness galaxies in the Fornax cluster

D. J. Prole,[1,2]★ M. Hilker,[1] R. F. J. van der Burg,[1] M. Cantiello,[3] A. Venhola,[4] E. Iodice,[5] G. van de Ven,[1] C. Wittmann,[6] R. F. Peletier,[7] S. Mieske,[8] M. Capaccioli,[5] N. R. Napolitano,[5] M. Paolillo,[9] M. Spavone[5] and E. Valentijn[7]

[1]*European Southern Observatory, Karl-Schwarzschild-Str 2, D-85748 Garching bei München, Germany*
[2]*School of Physics and Astronomy, Cardiff University, The Parade, Cardiff CF243AA, UK*
[3]*INAF-Osservatorio Astronomico d'Abruzzo, Via M. Maggini snc, I-64100 Teramo, Italy*
[4]*Division of Astronomy, Department of Physics, University of Oulu, FI-90014 Oulu, Finland*
[5]*INAF-Astronomical Observatory of Capodimonte, via Moiariello 16, I-80131 Naples, Italy*
[6]*Astronomisches Rechen-Institut, Zentrum für Astronomie der Universität Heidelberg, Mönchhofstraße 12-14, D-69120 Heidelberg, Germany*
[7]*Kapteyn Astronomical Institute, University of Groningen, PO Box 72, NL-9700 AV Groningen, the Netherlands*
[8]*European Southern Observatory, Alonso de Cordova 3107, Vitacura, Chile*
[9]*University of Naples "Federico II", C.U. Monte Sant'Angelo, Via Cinthia, I-80126 Naples, Italy*

Accepted 2019 January 28. Received 2019 January 22; in original form 2018 December 28

ABSTRACT

The halo masses $M_{\rm halo}$ of low surface brightness (LSB) galaxies are critical measurements for understanding their formation processes. One promising method to estimate a galaxy's $M_{\rm halo}$ is to exploit the empirical scaling relation between $M_{\rm halo}$ and the number of associated globular clusters ($N_{\rm GC}$). We use a Bayesian mixture model approach to measure $N_{\rm GC}$ for 175 LSB [$23 \leq \langle\mu_{e,r}\rangle$ (mag arcsec^{-2}) ≤ 28] galaxies in the Fornax cluster using the Fornax Deep Survey data; this is the largest sample of low-mass galaxies so-far analysed for this kind of study. The proximity of the Fornax cluster means that we can measure galaxies with much smaller physical sizes [$0.3 \leq r_{\rm e,r}$ (kpc) ≤ 9.5] compared to previous studies of the GC systems of LSB galaxies, probing stellar masses down to $M_* \sim 10^5$ M$_\odot$. The sample also includes 12 ultra-diffuse galaxies (UDGs), with projected r-band half-light radii greater than 1.5 kpc. Our results are consistent with an extrapolation of the M_*–$M_{\rm halo}$ relation predicted from abundance matching. In particular, our UDG measurements are consistent with dwarf-sized haloes, having typical masses between 10^{10} and 10^{11} M$_\odot$. Overall, our UDG sample is statistically indistinguishable from smaller LSB galaxies in the same magnitude range. We do not find any candidates likely to be as rich as some of those found in the Coma cluster. We suggest that environment might play a role in producing GC-rich LSB galaxies.

Key words: galaxies: clusters: individual: Fornax – galaxies: dwarf.

1 INTRODUCTION

Low surface brightness (LSB) galaxies are among the most common in the Universe, yet observational challenges (Disney 1976) mean that they are also among the most mysterious. The existence of large LSB galaxies is a well-known phenomenon. They were first detected several decades ago (e.g. Sandage & Binggeli 1984; Bothun et al. 1987; Impey, Bothun & Malin 1988) but have received renewed interest in more recent years. However, their intrinsic properties and formation histories are still not fully understood and it is not clear whether they represent a distinct population from smaller LSB dwarf galaxies, which can form naturally in high-spin haloes expected from hierarchical galaxy formation models (e.g. Dalcanton, Spergel & Summers 1995; Jimenez et al. 1998) and from harassment of normal dwarf galaxies (Moore, Lake & Katz 1998; Mastropietro et al. 2005).

An outstanding question is whether there is truly anything unique about the way in which large LSB galaxies form in comparison to their smaller counter-parts, given that they seem to share a continuous distribution of observable properties (Conselice, Gallagher & Wyse 2003; Wittmann et al. 2017; Conselice 2018). Since van Dokkum et al. (2015) detected a surprisingly high abundance of large LSB galaxies (that they termed ultra-diffuse galaxies or UDGs)

★ E-mail: danjampro@sky.com

in the Coma Cluster, numerous theories have been proposed to explain their origins. Initially, van Dokkum et al. (2015) suggested they could reside in massive haloes, similar in total mass to the Milky Way with a truncated star formation history. This is referred to as the 'failed L⋆' scenario, and is supported observationally by their unusually large sizes (optical effective radii $\geq$1.5 kpc) together with their LSB ($\mu_0^g \geq\sim 23$), red colours and abundance in dense environments.

There are several possible mechanisms to explain the existence of UDGs other than the failed L⋆ scenario. Yozin & Bekki (2015) have shown that ram-pressure stripping resulting from an early in-fall to cluster environments is sufficient to reproduce several properties of the Coma UDGs. Other authors have shown that different environmental effects like tidal heating may be enough to explain their formation (Collins et al. 2013; Carleton et al. 2018). While these models may seem to indicate that UDGs are phenomena associated preferentially with dense environments (supported observationally by van der Burg et al. 2017) (but see also Mancera Piña et al. 2018), it is also thought that a field population should exist (McGaugh 1996; Di Cintio et al. 2017), plausibly arising from the high angular momentum tail of the dwarf galaxy population (Amorisco & Loeb 2016) or from secular evolution processes such as supernovae feedback. Of course, there could be multiple formation scenarios for UDGs that combine both secular and environmentally driven processes (Jiang et al. 2018).

The halo mass is a key parameter in distinguishing between formation models of UDGs. Typically, current models favour dwarf-sized haloes with truncated star formation histories (e.g. Amorisco & Loeb 2016; Rong et al. 2017), making them similar to normal LSB galaxies but larger. UDGs are abundant in high-density environments such as in the centres of clusters (e.g. Koda et al. 2015; Mihos et al. 2015; Venhola et al. 2017) where they require a relatively high dark matter fraction in order to survive. However, it is not clear whether UDGs can form with lower mass-to-light ratios (M/L) in less dense environments such as the field (Trujillo et al. 2018; van Dokkum et al. 2018).

There have been several attempts to constrain the halo masses of UDGs with a variety of measurement techniques used, mainly focussing on UDGs in groups and clusters. Metrics include weak lensing (Sifón et al. 2018), prevalence of tidal features as a function of cluster radius (Mowla et al. 2017), comparisons of their spatial distribution with that of dwarf and massive galaxies (van der Burg, Muzzin & Hoekstra 2016; Román & Trujillo 2017), richness of their globular cluster systems (Beasley & Trujillo 2016; van Dokkum et al. 2017; Amorisco et al. 2018; Lim et al. 2018) as well as direct measurements of the velocity dispersions of stellar populations (van Dokkum et al. 2016) and globular cluster systems (Beasley et al. 2016; Toloba et al. 2018).

Globular clusters offer an interesting insight into the formation mechanisms of LSB galaxies. They are thought to form mainly in the early epochs of star formation within massive, dense giant molecular clouds that are able to survive feedback processes that might otherwise shut off star formation in their host galaxy (Hudson, Harris & Harris 2014; Harris, Blakeslee & Harris 2017). The halo mass of galaxies has been shown to correlate well with both the number of associated GCs ($N_{\rm GC}$) and the total mass of their GC systems ($M_{\rm GC}$; e.g. Spitler & Forbes 2009; Harris, Harris & Alessi 2013; Harris et al. 2017), which means measurements of either $N_{\rm GC}$ or $M_{\rm GC}$ can be used to constrain $M_{\rm halo}$. However, Forbes et al. (2018) show that the traditional relation between $N_{\rm GC}$ and $M_{\rm halo}$ may lose accuracy in the low $M_{\rm halo}$ regime, perhaps because lower mass galaxies tend to have lower mass GCs without a common mean GC mass. Additionally, it has been shown that there is a correlation between the GC half-count radius and $M_{\rm halo}$ (Forbes 2017; Hudson & Robison 2018).

The majority of studies of the GC populations of UDGs have up until now focused on the Coma galaxy cluster, the most massive ($M_{\rm tot} \sim 6 \times 10^{14}\,{\rm M}_\odot$, Hughes 1998) galaxy cluster within 100 Mpc. In this paper we analyse exclusively galaxies in the core of the Fornax cluster. In comparison to Coma, it is around five times closer ($d \sim 20$ Mpc, Blakeslee et al. 2009) but less massive ($M_{\rm tot} \sim 7 \times 10^{13}\,{\rm M}_\odot$, Drinkwater, Gregg & Colless 2001). Using the empirical relation of van der Burg et al. (2017), there are approximately 10 times less UDGs expected in Fornax than in Coma, many of which have been catalogued already (Muñoz et al. 2015; Venhola et al. 2017).

While overall we have a relatively small sample of UDGs, an advantage of working with the Fornax cluster is that cluster members have much larger projected sizes compared to the background galaxy population, so we can analyse the population of smaller LSB galaxies at the same time as the UDG population without contamination from interlopers. Indeed, much of the new literature surrounding LSB galaxies focuses on UDGs and this may be in-part due to the relative ease of distinguishing larger galaxies from background objects in group or cluster environments. A second advantage of Fornax over Coma is that GCs are brighter in apparent magnitude by ∼3.5 mag due to their relative proximity, meaning that we can probe further into the GC luminosity function.

We note that the relatively large number of galaxies we analyse in this study is important for at least partially overcoming systematic uncertainties involved in measuring halo masses with low numbers of tracers as made clear by Laporte, Agnello & Navarro (2018) and the possible stochastic nature of the $M_*-M_{\rm halo}$ relation at low mass (Brook et al. 2014; Errani, Peñarrubia & Walker 2018).

In this work we provide constraints on the halo masses for a selection of LSB galaxies first identified by Venhola et al. (2017) using the optical Fornax Deep Survey (FDS, Iodice et al. 2016). The structure of the paper is as follows: We describe the data in Section 2. In Section 3 we describe the method to detect globular cluster candidates (GCCs) and infer the total number of GCs associated with our target galaxies. We provide our results in Section 4, where we estimate the halo masses from the inferences on $N_{\rm GC}$ and $M_{\rm GC}$ using the empirical scaling relations of Harris et al. (2017). We discuss our results and provide conclusive remarks in Section 5. We use the AB magnitude system throughout the paper, and adopt a distance of 20 Mpc to the Fornax cluster.

2 DATA

We use the four central 1×1 deg^2 frames of the FDS (FDS IDs 10, 11, 12, and 16), i.e. the same region used by Venhola et al. (2017) in their by-eye classification of low surface brightness sources in the Fornax galaxy cluster. These data were obtained using the OmegaCAM (Kuijken 2011) instrument on the 2.6m ESO VLT Survey Telescope (VST, Capaccioli et al. 2012) in the u', g', r', and i' bands. We note that Fornax GCs are unresolved in our data such that we consider them as point sources throughout the paper.

We specifically used the VSTtube-reduced FDS data (Grado et al. 2012; Capaccioli et al. 2015), which is optimized for point-source photometry but is not as deep as the data used by Venhola et al. (2017), which is reduced using a combination of the OmegaCAM pipeline and AstroWISE (McFarland et al. 2011), but with a slightly wider point spread function (PSF) than the VST-tube reduction because images with poor seeing were included in the stacks.

Table 1. PROFOUND measurement constraints for point source selection in the PSF modelling. `axrat` is the axial ratio. `Nobject` is the number of pixels belonging to the segment that are touching another source. `Nmask` is the number of pixels belonging to the segment that are touching a masked region. See the PROFOUND documentation for more details of these parameters. Further criteria are discussed in the text.

Parameter	Constraint
`mag` (g)	14–19 (mag)
`axrat`	≥0.95
`Nobject`	0
`Nmask`	0

We also performed additional photometric corrections to bring our photometry into the AB magnitude system as described in Appendix B.

3 METHODOLOGY

In this work we target the GC populations of galaxies identified by-eye in the (Venhola et al. 2017, hereafter V17) catalogue. We split the sample into two groups: low surface brightness galaxies (LSBGs), defined as those with r-band effective radii $r_{e,r} < 1.5$ kpc and UDGs, defined as those with $r_{e,r} \geq 1.5$ kpc. The sources are defined as LSB because they were measured to have central surface brightness $\mu_0^r \geq 23$ by V17. We omit two UDGs (FDS11_LSB1 and FDS11_LSB17) from the sample because they are in significantly crowded locations and measuring their properties accurately would require a more sophisticated analysis.

Before running our detection algorithm, we subtract model galaxy profiles in each band using IMFIT (Erwin 2015, see Appendix A). We were unable to get a stable IMFIT model for three sources (FDS11_LSB16, FDS12_42, FDS12_47) because they were too faint, so we adopt the measurements of V17 (made from deeper stacks) for these sources and rely on a separate background subtraction procedure to remove the galaxy light (see Section 3.3). We select only galaxies with measured r-band effective radii greater than 3 arcsec (∼0.3 kpc at Fornax distance) so that we target cluster members with confidence (Sabatini et al. 2003; Davies, Davies & Keenan 2016).

We used the PROFOUND[1] package (Robotham et al. 2018) for the source detection and photometry, with the following settings: `box = 100` pixels (∼20 arcsec), `sigma = 2` pixels, `threshold = 1.03`, `tolerance = 1`, `skycut = 1`. All other settings were defaults. Our detection was performed exclusively on the g band (the deepest) so that we could easily measure and account for our detection efficiency without considering the colours of individual sources. We note that we split the four FDS frames into 9 × 9 subframes to ease the memory requirements for PROFOUND.

3.1 PSF models

We obtained PSF models for each band and subframe using our PROFOUND measurements as follows. Bright, unsaturated point sources were selected in the PROFOUND `mag - R50` (approx. half-light radius) plane, using the selection criteria listed in Table 1. Additionally we sigma-clipped the measurements in `R50` (approximately flat over the magnitude range for point sources) and offset the relation by 4σ with respect to the median to measure an upper limit on `R50` for the selection.

We used IMFIT to fit a model Moffat profile (keeping the axial ratio as a free parameter) to each point source following a local sky subtraction. We did not stack individual point source cut-outs to avoid artificial widening of the PSF caused by misalignment of the images. The resulting distribution of model Moffat fits was then sigma-clipped at 3σ in the FWHM-concentration index plane to remove outliers caused by bad fits. We finally selected a fiducial model PSF for each band and subframe by adopting the fit with the average full width at half-maximum (FWHM).

Of primary importance for our analysis are the g-band PSF models. While for a specific FDS frame we found little variation of the PSF over its subframes, on a frame-by-frame basis the IMFIT FWHM ranges between approximately 0.7 and 1.2 arcsec.

3.2 Point source selection

We used synthetic source injections based on our Moffat PSF models from Section 3.1 to produce our point source selection function and quantify our recovery efficiency (RE). We injected ∼25 000 synthetic profiles per subframe into the real data at random locations in the vicinities (420 arcsec × 420 arcsec cut-outs) of our target galaxies after subtracting the galaxy models from the data. This was done in the g band, with apparent magnitudes ranging between 19 and 26. Our matching criteria for the synthetic sources was that the central coordinate of the injected source had to lie on top of a segment in the PROFOUND segmentation map. Additionally, we only considered sources that did not match with segments from the result of running PROFOUND over the original frames (i.e. without the injected sources). We note that the measurements of the synthetic point sources are in good agreement with measurements of real sources when plotted on the `mag-R50` plane.

Once we had acquired the PROFOUND measurements of the synthetic sources, we fitted a smooth cubic spline to the data in the PROFOUND `mag` and `R50` plane. Specifically, the spline was fitted to the data binned in `mag`, and positively offset by 4σ of the `R50` values within the bin (see Fig. 1). The rationale behind this was that as sources become fainter, the scatter in `R50` increases such that a simple cut at a specific value would be either too high for bright objects or conversely too low for some of the fainter objects with large values of `R50`. We obtained a different point source selection function for each subframe.

3.3 Colour measurement

We obtained aperture magnitudes of the PROFOUND sources in fixed apertures of diameter 5 pixels in all the bands. The sky level and its uncertainty were calculated for each detected source by placing many identical apertures in 51 × 51 pixel cut-outs (the fiducial FWHM of 1 arcsec is ∼5 pixels) and recording the median and standard deviation of the contained flux values after sigma-clipping these at 2σ to remove contamination from other sources. Additionally the sky apertures were placed at radii greater than 20 pixels from the centre of the source.

These magnitudes were then corrected for the PSF size in each band through calibration against an existing catalogue of PSF-corrected point sources made using the same data (Cantiello et al. in preparation). See Appendix B for a discussion of the photometric calibration procedure. We note that we have not used this catalogue for this work because of the need to subtract galaxy profiles from the data and the need to quantify the RE.

[1] https://github.com/asgr/ProFound

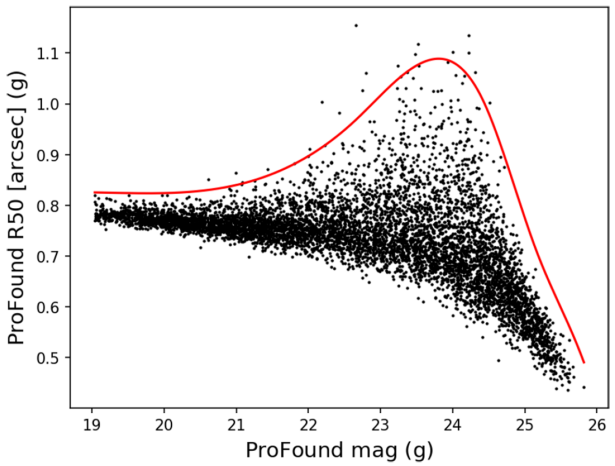

Figure 1. Point source selection function for a subframe (red line) obtained by fitting a cubic spline to measurements from the synthetic source injections (black points) after offsetting `R50` by 4σ in bins of magnitude with respect to the median. All points lower than the red line are selected. The increase in scatter towards the faint end means that a simple cut in `R50` would result in either a low RE or a high level of contamination from our point source selection.

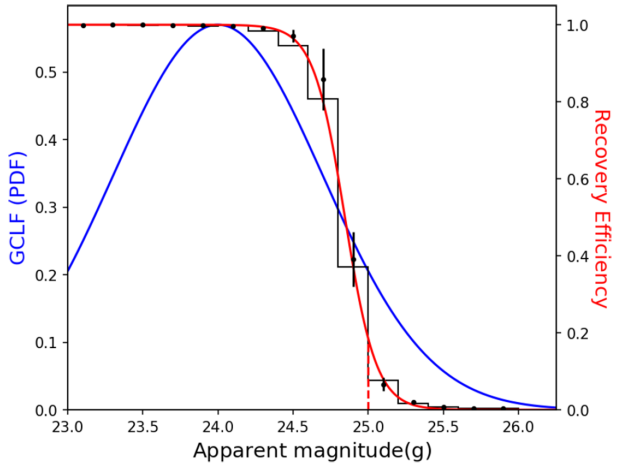

Figure 2. g-band RE for a subframe of injected point sources (black histogram) after applying our selection criteria, along with the RE (red line) and a fiducial GCLF (blue line). The dashed red line shows our additional cut at $m_g = 25$. The GCLF turnover magnitude is clearly reached by our detection pipeline. Integrating the RE over the GCLF (including the magnitude cuts) yields an overall RE of ∼80 per cent. Also shown is the mean and standard deviation of the RE across all the subframes for FDS frame 10 (black error bars).

3.4 Recovery efficiency

We quantified the RE separately for each subframe using the point source selection functions with the synthetic source measurements. We imposed a faint-end limit on the corrected g-band aperture magnitude of 25 mag because measuring accurate colours at fainter magnitudes is more difficult and because the degeneracy between point sources and other faint sources in the `mag-R50` plane is exacerbated in this region. Additionally, we apply a lower bound cut in the corrected g-band aperture magnitude of 21 mag to reduce possible contamination from bright stars, ultra-compact dwarf galaxies (UCDs) and nuclear star clusters (NSCs).

The RE itself was measured by taking the ratio of detected and selected point source injections to the total number of injected sources in bins of intrinsic magnitude. A sigmoid function,

$$\epsilon(m) = [1 + \exp(-k_1(k_2 - m))]^{-1} \quad (1)$$

was fit to the result (see Fig. 2). The RE $\varepsilon(m)$ is sufficient to reach the turnover magnitude of the g-band GC luminosity function (GCLF), which is approximated by a Gaussian function centred at $24m_g$ at the distance of Fornax (Villegas et al. 2010). We adopt a value of 0.7 for the GCLF standard deviation, which is a reasonable estimate for low surface brightness galaxies (Trujillo et al. 2018). Under these assumptions, our estimated GC completeness ranges between ∼60 per cent and 90 per cent depending on the subframe. The mean completeness is estimated to be 82 per cent across all the subframes. Of course, this number depends on the exact form of the adopted GCLF. While its peak at $24m_g$ is fairly well known (The peak of the GCLF can sometimes be used as a standard candle, see Rejkuba 2012.), a degree of uncertainty is attributed to its width. We discuss the effects of varying the GCLF on our results in Section 4.6.

3.5 Colour selection

We have applied a colour selection to our point sources to produce a catalogue of GCCs for each target galaxy, using as few assumptions about the underlying GC colours as possible. The full colour space in u, g, r, i was used for the selection. This is important because of the need to remove interloping point sources from our final GCC catalogue, which include foreground stars and unresolved background galaxies. However, we point out that both interloping populations are partially degenerate in colour space with the actual GCs (see also Pota et al. 2018) and these sources must be accounted for using spatial information (see Section 3.6).

This colour selection was accomplished by first cross-matching our point sources from the four FDS frames with a compilation of spectroscopically confirmed Fornax compact objects (Schuberth et al. 2010; Wittmann et al. 2016; Pota et al. 2018). This resulted in a catalogue of 992 matching sources. We note that we partially account for bright UCDs with our bright-end magnitude cut-off. The external catalogue has a magnitude distribution that drops off quickly at magnitudes fainter than $\sim 23m_g$ and so is not complete for our purposes and this limited depth has to be accounted for.

We used the density-based clustering algorithm `DBSCAN` (Ester et al. 1996) to define regions in the $(u - g) - (g - r)$ and $(g - r) - (g - i)$ planes separately for our GCC selection. We used a clustering radius of 0.1 mag and required at least five spectroscopic GCs within this radius for clusters to form. After acquiring the DBSCAN clusters, we fitted a convex hull to all the clustered points and used this as the boundary of the selection box; the results of this are shown in Fig. 3. Approximately 93 per cent of the spectroscopic GCs occupy the selection region and we correct for this factor in our later inferences on N_{GC}.

The fraction of GCs that occupy the colour selection box decreases as a function of magnitude because of measurement error. Thus, we have used a probabilistic approach to identify all sources that *could* occupy the box, given their uncertainty. Specifically, we selected all sources that were consistent within 2σ of their measurement uncertainty of the box, separately in each colour–colour plane. While the colour selection box was measured in magnitude units, we actually converted it into linear flux-ratio units (accounting for the photometric calibration) to select GCCs. This was done primarily to overcome the effects of the shallow u band which would otherwise impact our estimate of the RE. A visual

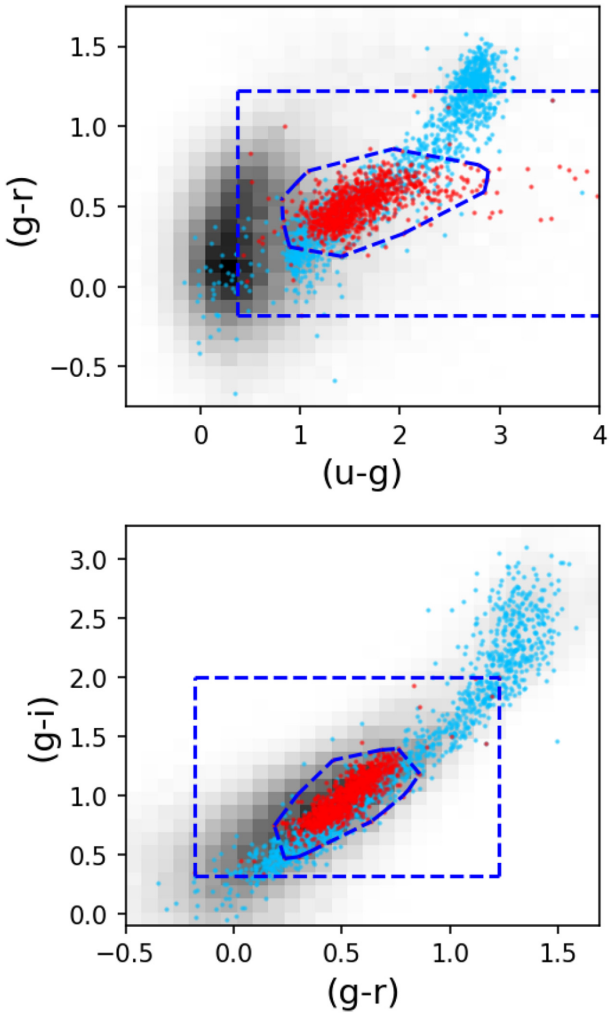

Figure 3. Colour–colour measurements of spectroscopic Fornax compact objects (red points), galactic stars (blue points) against the empirical distribution of all detected point sources over a subframe (greyscale histogram). Also shown are two colour selection boxes (blue dashed lines). In each panel, the large box corresponds to the minimum-bounding rectangle of compact object measurements in this colour–colour plane, and the smaller box is produced using the DBSCAN algorithm.

example of our combined point source selection criteria with colour selection for one of our target galaxies is shown in Fig. 4.

We also performed a separate analysis using a much wider colour-selection box, also shown in Fig. 3. We measured the minimum bounding rectangles in each colour–colour plane from the matching sources, forming a 3D colour selection box. The box is bounded by $-0.18 < (g - r) < 1.23$, $0.32 < (g - i) < 2.00$, $0.37 < (u - g) < 5.07$; the high upper limit on $(u - g)$ is likely due to scatter caused by the shallow u band. While conservative in nature, the box is sufficient to contain all the matching spectroscopic GCs down to $m_g \sim 23$. We note here that our overall results are not significantly impacted by this change. We refer to the results obtained using the DBSCAN colour box for the remainder of the paper.

We note that we do not fit for the intrinsic colour distribution of GCs and interlopers as was done in Amorisco et al. (2018). The reason for this is that simple statistical representations (e.g. Gaussian) are inappropriate to describe our data in the multidimensional colour space. This can be gathered from the appearance of Fig. 3. It

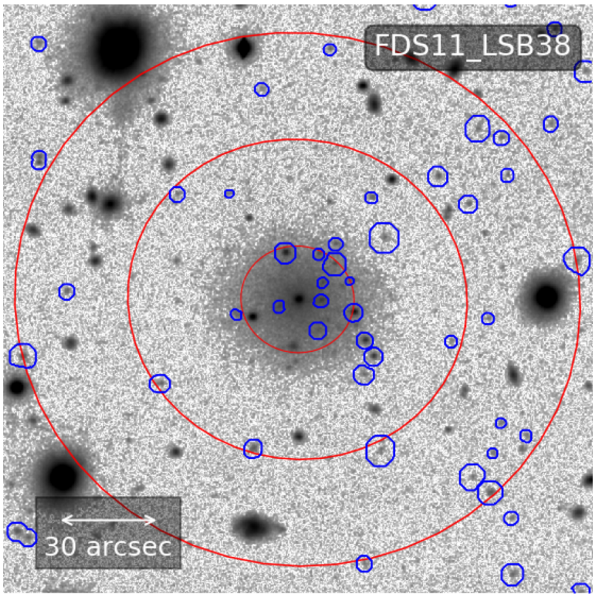

Figure 4. Result of full GCC identification and selection for one of our target galaxies. The selected sources are shown using their PROFOUND segments in blue. We also show the 1, 3, and 5 $r_{e,r}$ contours from the IMFIT modelling. A clear overdensity of sources can be seen close to the centre of the galaxy.

may be possible to include extra colour-terms in the mixture models described in Section 3.6, but we leave this for future work.

3.6 Bayesian mixture models

We adopt a simplified version of the Bayesian mixture modelling of Amorisco et al. (2018) to measure the properties of the GC systems of our target galaxies. We are similarly motivated to rescale the spatial coordinates of the GCCs into units of the $1r_{e,r}$ (half-light radius of the galaxy) ellipse. Our model consists of two surface density components: a central Plummer profile to represent the GCs associated with the target galaxy,

$$\Sigma(r, r_h) = \frac{1}{\pi} \frac{1}{r_h^2(1 + r^2/r_h^2)^2} \tag{2}$$

where r_h is the half number radius, in units of $r_{e,r}$, and a uniform distribution to represent the background, which mainly consists of stars, background galaxies, and intra-cluster GCs. The presence of NGC 1399 in the centre of Fornax means that its GC system may contribute to a non-uniform background in its vicinity. However, it can be shown that for our galaxies the gradient in the surface density of GCs belonging to NGC 1399 is negligible, with a maximal gradient value of $\sim 10^{-4}$ objects arcmin^{-3} in the vicinity of our sources. For this calculation, we have used the de Vaucouleurs' fit to the GC system of NGC 1399 from Bassino et al. (2006). The total model likelihood takes the form:

$$\mathcal{L} = \prod_{i=1}^{N_{GCC}} \left[\frac{f\,\Sigma(r_i, r_h)}{\int_0^{r_{max}} S(r')\Sigma(r', r_h) r'\,dr'} + \frac{1 - f}{\int_0^{r_{max}} S(r') r'\,dr'} \right], \tag{3}$$

where i runs over all detected (and not masked) GCCs within the transformed radius r_{max} of the galaxy, which we fix as $15r_{e,r}$; large enough to include all the galaxies' GCs and a large number of background GCCs. We do not consider larger regions because of the increased potential of contamination from steep GCC gradients in the Fornax core. The spatial completeness function $S(r)$ encodes

the fractional unmasked area as a function of radius. There are two free parameters: f, the mixing fraction (i.e. the fraction of all sources that are GCs belonging to the target galaxy) and the ratio $r_{\rm h}/r_{\rm e}$. We do not explicitly include morphological or colour terms in the model likelihood, but account for this in the GCC selection described in Sections 3.2 and 3.5.

We impose a Gaussian prior on the ratio $r_{\rm h}/r_{\rm e}$ based on the results of Amorisco et al. (2018). The prior is centred at $\sim$1.5$r_{\rm e}$ with a standard deviation of 0.8 and truncated at zero. The choice of prior is very influential, particularly in the low f regime in which most of our sources are anticipated to lie. However, since Amorisco et al. (2018) probe a similar sample of sources in a similar environment (the Coma cluster) to ours and that the $r_{\rm h}/r_{\rm e} \simeq 1.5r_{\rm e}$ relationship appears elsewhere in the literature (van Dokkum et al. 2017; Lim et al. 2018) it is a reasonable estimate. We probe the effects of modifying the prior on $r_{\rm h}$ in Appendix D. The prior width is much greater than the RMS of the median values quoted by Amorisco et al. (2018), so that if there is any significant deviation it should be recognized in our analysis.

4 RESULTS

4.1 Inference on globular cluster numbers

We made data cut-outs in each band for each source that were 15 × 15 $r_{\rm e,r}$ in size. We chose this size because tests with mock datasets (with realistic numbers of interlopers derived from the data) revealed that the measured number of GCs was negatively biased for much smaller values, and this particularly affected systems with less than 10 intrinsic GCs. At 15 × 15 $r_{\rm e,r}$, we were able to recover unbiased measurements of $N_{\rm GC}$ even for systems with no GCs.

The GCCs were selected according to the criteria described in Section 3.2 and by their colour, described in Section 3.5. All non-selected sources were masked using their PROFOUND segments. We additionally automatically masked the areas around PROFOUND sources with g-band magnitudes brighter than 19 in an effort to remove interloping GCs belonging to other systems. This was accomplished by placing elliptical masks scaled to two times the PROFOUND `R100` radius.

All sources in the GCC catalogues that had central coordinates overlapping with the masks were removed. The spatial completeness function could then be measured by measuring the masked fraction in concentric annuli centred on the galaxy, spaced by 0.01$r_{\rm e,r}$ and linearly interpolating the result. We note that two sources[2] were omitted from the analysis because they were almost completely masked.

We then ran the Monte Carlo Markov chain (MCMC) code EMCEE[3] to obtain the posterior distributions of f and $r_{\rm h}$ for each individual target galaxy. The final inference on the number of GCs associated with each galaxy, $N_{\rm GC}$, was calculated as

$$N_{\rm GC}^{j} = f^{j}\,\frac{\int_0^{r_{\rm max}} \Sigma(r, r_{\rm h}^{j}) r\,{\rm d}r}{\int_0^{r_{\rm max}} S(r)\Sigma(r, r_{\rm h}^{j}) r\,{\rm d}r}\,\frac{\int_{m_1}^{m_2} g(m)\,{\rm d}m}{\int_{m_1}^{m_2} \epsilon(m) g(m)\,{\rm d}m}\,N_{\rm GCC} \qquad (4)$$

taking into account the masked fraction and magnitude incompleteness. Here, j indicates the posterior index and $g(m)$ is the Gaussian g-band GCLF. The results of this are shown in Fig. 5, where we convert our galaxy photometry to V-band magnitudes using the prescriptions of Jester et al. (2005). As a means of comparison, we show in Appendix C that our inferences on $N_{\rm GC}$ are consistent with the measurements of Miller & Lotz (2007) for a small sample of overlapping galaxies using a chi-squared test.

We record the following information from the $N_{\rm GC}$ posterior: The 10th, 50th, and 90th percentiles, the 15.9 and 84.1 percentiles (i.e. the 1σ limits centred on the median). The numbers we quote for $N_{\rm GC}$ are the median values and the uncertainties span the range of the 1σ limits centred on the median; these are the error bars shown in Fig. 5. Note that these estimates are corrected for the colour incompleteness from Section 3.5. We provide our measurements for the full sample of galaxies in Table E1. Trials with mock datasets showed that the median value is not significantly biased despite the marginal posterior in f being naturally truncated at zero by our model. We find that 0 out of 12 UDGs have median values of $N_{\rm GC}$ below one, compared to 12 across the whole sample. However, 106 of the whole sample of target galaxies are consistent with having no GCs within 1σ.

Overall, our results show a general increase of $N_{\rm GC}$ with M_V that is qualitatively consistent with normal dwarf galaxies. While some UDGs are comparable with those of van Dokkum et al. (2017), most of their objects are quite remarkable when compared to our measurements in terms of having much higher $N_{\rm GC}$ for a given luminosity. It remains to be seen whether these sources are comparatively rare among LSB galaxies and because Fornax contains less galaxies we see fewer UDGs with GC excess, or that perhaps the increase in environmental density in the Coma cluster plays a positive role in producing such galaxies; this is discussed further in Section 5.

4.2 Colours

Despite already imposing a conservative colour selection criterion in Section 3.5, we can use our results to assess the distribution of colour within the selection box. For each posterior sample, one can assign a probability of belonging to the Plummer profile (i.e. the galaxy) to each GCC given by

$$P_{\rm GC}(r)^{j} = \left[1 + \frac{2(1-f^{j})\int_0^{r_{\rm max}} \Sigma(r', r_{\rm h}^{j}) r'\,{\rm d}r'}{f^{j}\Sigma(r, r_{\rm h}^{j}) r^{2}}\right]^{-1}, \qquad (5)$$

where j loops over the posterior sample. The result of selecting high-probability GCCs is shown for a selection of galaxies in Fig. 6. We display the full colour distributions for all our GCCs weighted by their probabilities of cluster membership in Fig. 7. It is clear from these distributions that one-or-two-component Gaussian fits are inappropriate, so we limit ourselves to a qualitative discussion based on the weighted histograms.

Comparing the weighted $(g-i)$ histogram with the un-weighted version, it is clear that a narrow peak emerges that is coincident with the blue component measured by D'Abrusco et al. (2016) at $<g-i> = 0.74$. We conclude that the GC population of our sample is mainly blue. This is consistent with the results of Peng et al. (2006), who have shown that low-luminosity galaxies tend to have predominantly blue GC systems. The blue nature of the GCs is suggestive of young and/or low-metallicity stellar populations.

In Fig. 7 we also show the $\pm1\sigma$ span of the colours of the target galaxies. Clearly the blue peaks we observe in $(g-i)$ and $(g-r)$ are consistent with these colours. In $(g-r)$, the blue peak of the GCs appears shifted to the blue compared to the galaxy colours. However, since this effect is within the 1σ, it is not a significant result.

[2] FDS10_LSB33, FDS11_LSB32
[3] http://dfm.io/emcee/current/

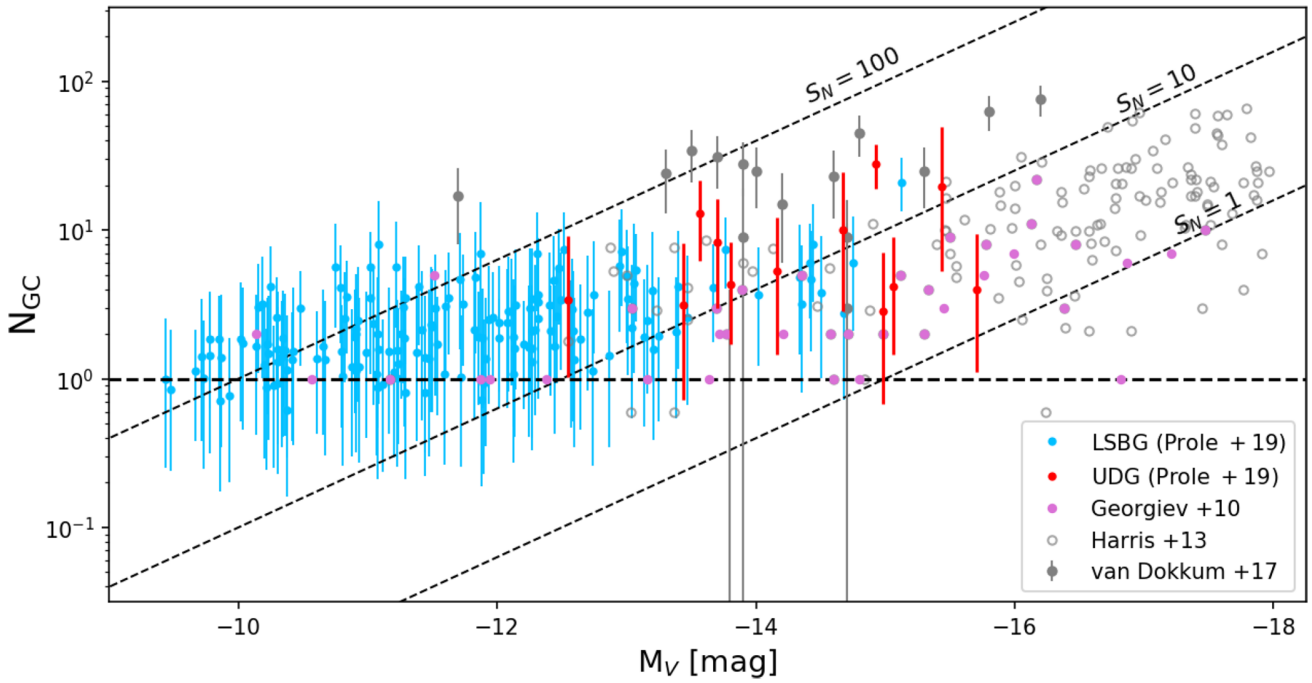

Figure 5. Corrected number counts of globular clusters as a function of absolute *V*-band magnitude. On the figure we show our new measurements in blue (LSBG sample) and red (UDG sample). The points represent median values from our MCMC posterior, and the error bars span the range of the 1σ uncertainties. The open grey circles belong to the Harris et al. (2013) catalogue. The grey points with error bars are the sample of selected Coma UDGs from van Dokkum et al. (2017). We also plot the sample of dwarf galaxies measured by Georgiev et al. (2010) in pink. The diagonal dashed black lines represent S_N contours, whereas the horizontal one represents 1 GC.

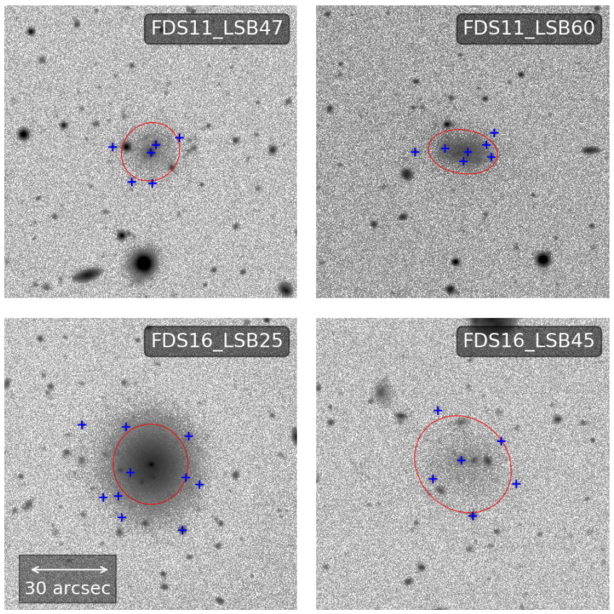

Figure 6. *r*-band cut-outs of four of our target galaxies, selected from galaxies with $N_{GC} \geq 5$. The red ellipses represent $1r_{e,r}$ contours. The blue points identify GCCs with $P_{GC} \geq 0.5$. Of the four galaxies shown, FDS16_LSB45 is the only one we measure to be large enough to be classified as a UDG. 30 arcsec is ∼2.9 kpc at Fornax distance.

4.3 Stellar mass versus halo mass

Using our estimates of N_{GC} together with the empirical trend of Harris et al. (2017) (accounting for the intrinsic scatter in the relation), we are able to estimate the halo mass M_{halo} of the sample of galaxies. For the estimate to be valid, one must assume that N_{GC} is indeed a reasonable indicator of M_{halo} in the LSB regime. There is limited evidence to support this (Beasley et al. 2016; van Dokkum et al. 2017) based on comparisons between M_{halo} measurements inferred from N_{GC} and those inferred from kinematic measurements. We also estimate the stellar mass using the empirical relation of Taylor et al. (2011) (their equation 8), who used the GAMA survey (Driver et al. 2011) to calibrate stellar mass as a function of *g* and *i* magnitudes with an intrinsic scatter of ∼0.1 dex.

We plot our estimates of M_{halo} versus M_* in Fig. 8. We also display other measurements from the literature, including the sample of Coma UDGs from van Dokkum et al. (2017) and the median values measured by Amorisco et al. (2018) (it is worth noting that only three of their sources have $M_{halo} > 10^{11}\,M_\odot$ at 90 per cent confidence), along with measurements of other dwarf galaxies, including dwarf ellipticals in clusters (Miller & Lotz 2007) as well as late-type dwarfs from a variety of environments including the field (Georgiev et al. 2010). We also show the 2σ credibility upper limit on the average mass of UDGs derived from weak lensing by Sifón et al. (2018), with which our results are consistent. Also we show the extrapolated theoretical predictions from abundance matching of Moster et al. (2010), Behroozi, Wechsler & Conroy (2013) and Brook et al. (2014), which were calibrated using observed stellar masses greater than approximately 10^8, 10^7, and $10^7\,M_\odot$, respectively.

Forbes et al. (2018) show that the N_{GC} to M_{halo} relation may lose accuracy for $M_{halo} \leq 10^{10}\,M_\odot$, giving systematically higher values of M_{halo} than measured for their sample. According to their study, a better estimator of M_{halo} is the total mass associated with the GC system; however, they note that the assumption of a common mean GC mass is not valid at the low-mass end such that individual GC masses should be measured to get an unbiased estimate of M_{halo},

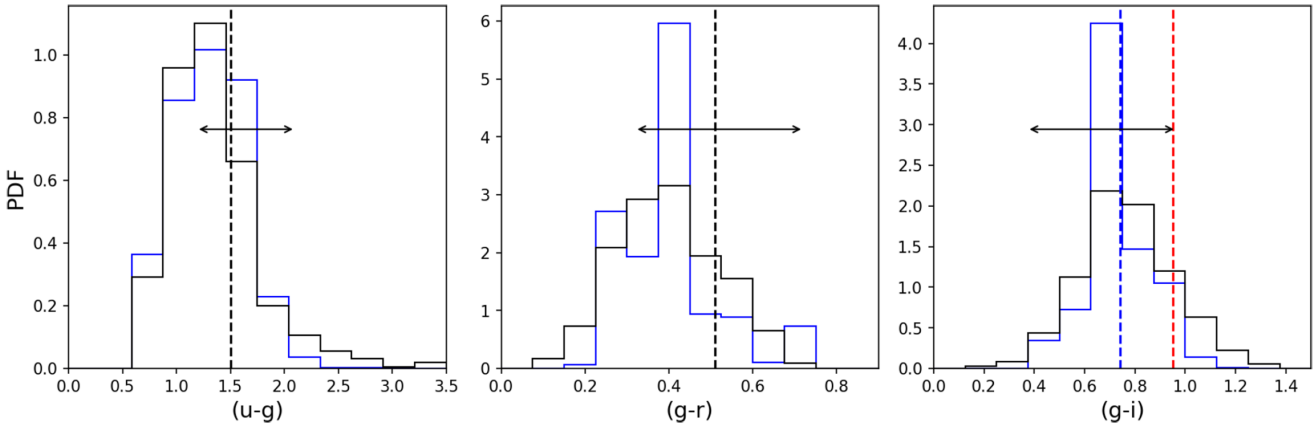

Figure 7. Normalized distribution of colours for the GCC sample (black histograms) versus those of the same sample after being weighted by their probability of belonging to a target galaxy's GC system according to equation (5) (blue histograms). We note that we select only sources with $m_g \leq 23$ to overcome the measurement error and ease comparison with D'Abrusco et al. (2016), who used a similar limit. For $(u - g)$ and $(g - r)$, the vertical black dashed lines correspond to the median colours of the sample of spectroscopic sources described in Section 3.5. The dashed blue and red lines in the $(g - i)$ panel correspond to the means of the blue and red components measured by D'Abrusco et al. (2016). The results a consistent with a predominantly blue GC population. The horizontal arrows indicate the $\pm 1\sigma$ range of the galaxy colours.

using the empirical relation of Spitler & Forbes (2009). While we have not measured the individual GC masses in this work, we note that our estimates of $M_{\rm halo}$ should be considered as upper limits in light of their result.

Every UDG in our sample is consistent with inhabiting a dwarf sized halo to within 1σ. There appears to be no significant tendency for UDGs to have enhanced GC populations and therefore enhanced halo mass for their stellar mass. Indeed, there is a qualitatively continuous trend from the LSBGs towards the UDGs.

The overall population is most consistent with an extrapolation of the Brook et al. (2014) relation (calibrated with Local Group dwarf galaxies), but we cannot rule out consistency with that of Moster et al. (2010) or Behroozi et al. (2013) because of the potential for our estimates of $M_{\rm halo}$ to be overestimates. We emphasize however that all models require extrapolation, below stellar masses of 10^8 M$_\odot$ for the Moster et al. (2010) relation, and 10^7 M$_\odot$ for that of Behroozi et al. (2013) and Brook et al. (2014).

While no UDGs have estimates of $M_{\rm halo}$ above what might be expected for enriched GC systems (according to the empirical relation of Amorisco et al. 2018), several of the LSBG sample do show evidence for excess. This might suggest a continuation of GC-enriched systems down to very low stellar mass.

Another point of interest is that our overall sample of LSB galaxies (including UDGs) appears offset from the mean trend of dwarf galaxies, having higher $M_{\rm halo}$ for a given M_*. While our estimates of M_* for the objects from the literature require assumptions about their colours, this may hint that LSB galaxies have systematically higher M/L ratios than normal dwarfs. However this might be a systematic effect; perhaps only LSB galaxies of high M/L ratio are able to survive in the Fornax core.

4.4 GC system sizes

Despite imposing a prior on $r_{\rm h}$ (the GC half number radius) with a mean of $1.5r_e$, we find that our GC systems are typically slightly larger. The median value of $r_{\rm h}$ recovered from the full sample of galaxies is 1.73, with a standard deviation of $\sim$0.27 and range between 0.4 and 2.8 (in units of $r_{\rm e,r}$). We note that the median value of $r_{\rm h}$ for the UDGs is consistent with that of the full sample.

If we use the relation between $r_{\rm h}$ and $M_{\rm halo}$ presented in Hudson & Robison (2018), the resulting $M_{\rm halo}$ estimate is much larger than previously estimated using $N_{\rm GC}$. For example, for an UDG with $r_{\rm h} = 1.5$ kpc should have $M_{\rm halo}$ of around $10^{11.6}$ M$_\odot$, much higher than many of the estimates presented in Fig. 8 and generally inconsistent with UDGs with halo mass measurements in the literature (e.g. van Dokkum et al. 2017). While we note that Hudson & Robison (2018) make clear that the relation is calibrated only for $M_{\rm halo} \geq 10^{12}M_\odot$, we advocate a relation more in-line with that of Forbes (2017) in this regime.

4.5 LSBGs versus UDGs

Now that we have estimates of $N_{\rm GC}$ for each of our target galaxies, we are in a position to directly compare the LSBG population with the UDGs. The two questions we want to answer are: Does the UDG population show any statistical excess of GCs when compared with the LSBGs in the same luminosity range?; and, is the observed distribution of $N_{\rm GC}$ for the UDGs discontinuous from that of the LSBGs?

We note that from the appearance of Fig. 5, it seems that $N_{\rm GC}$ versus M_V can be modelled approximately as a power law. We omit all UDGs from the sample and fit such a relation to our LSBG sample (see also Fig. 9):

$$\bar{N}_{\rm GC} = (0.04 \pm 0.02) \times 10^{(-0.15 \pm 0.02) \times M_V}. \quad (6)$$

We note that the scatter in the relation is approximately 0.2 dex across the full magnitude range. Using the fit, we can ask whether our sample of UDGs (ignoring other UDGs from the literature) are consistent with this description. We perform a chi-squared test with the null-hypothesis that the UDGs are drawn from equation (6). This results in a p-value of 0.30, which means we cannot reject the null hypothesis with an acceptable level of confidence. We therefore conclude that our UDG sample is quantitatively consistent with a continuation of the LSBG sample in this parameter space. We also note that since there is no UDG that has a $N_{\rm GC}$ measurement convincingly more than 3σ above the power-law predicted value, there is no compelling evidence that our UDGs have excessive GC populations.

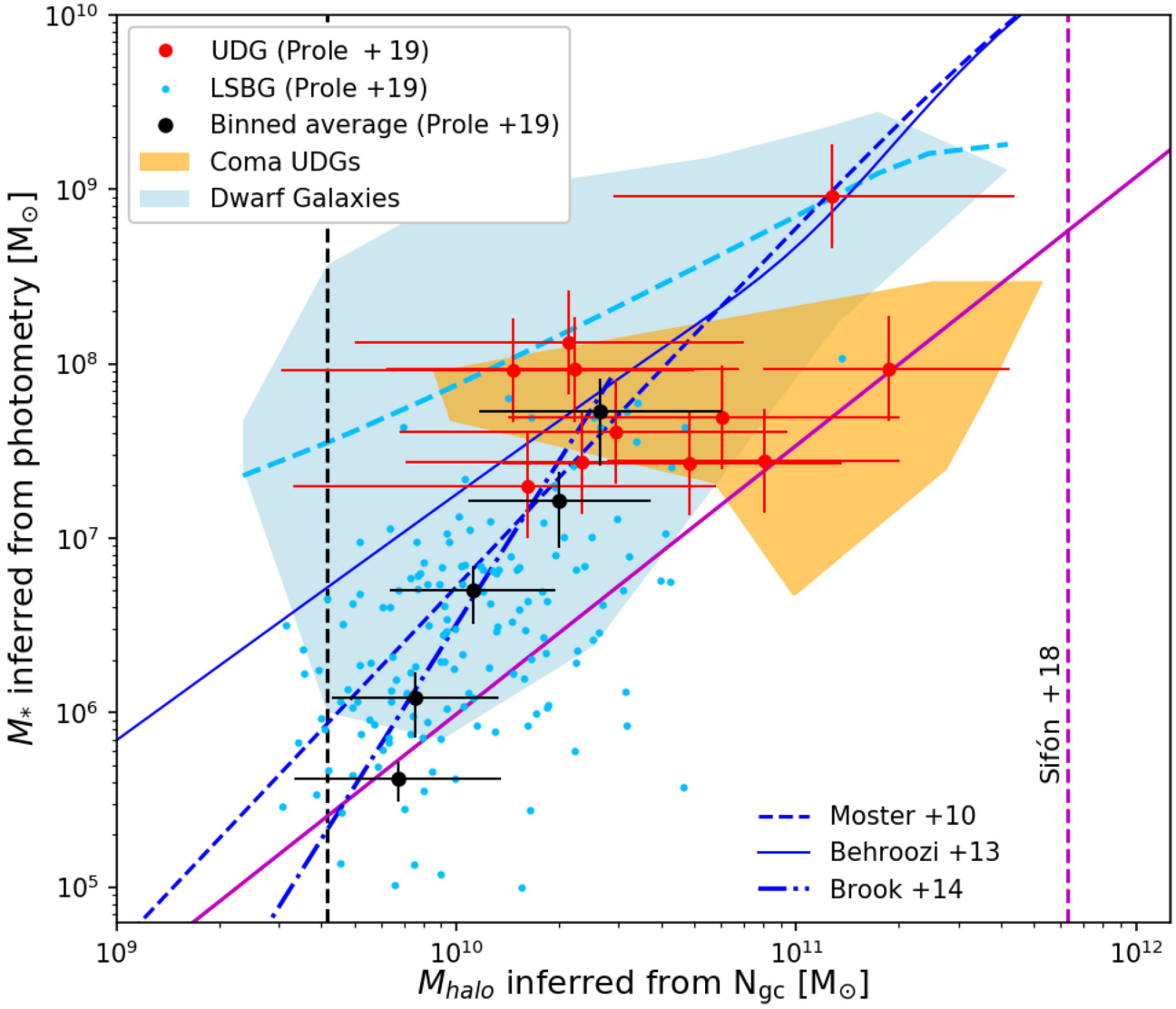

Figure 8. Halo mass (derived using N_{GC}) versus stellar mass. In the figure we show our new measurements, the light blue points correspond to LSBGs and the red to UDGs. The stellar masses for our points were derived from *g*- and *i*-band photometry using the scaling relation of Taylor et al. (2011). The black error bars show illustrative binned averages of all our new measurements (calculated in logarithmic bins). The orange region bounds UDG measurements from the literature (van Dokkum et al. 2017; Amorisco et al. 2018; Lim et al. 2018), We also plot measurements of other 'normal' dwarf galaxies (Miller & Lotz 2007; Georgiev et al. 2010, blue region). The dashed light blue line represents the mean of these sources. The darker blue lines show extrapolated theoretical predictions of Moster et al. (2010), Behroozi et al. (2013), and Brook et al. (2014). The diagonal purple line corresponds to 'enhanced' GC systems Amorisco et al. (2018), using the Harris et al. (2017) conversion between N_{GC} and M_{halo}. The dashed purple line indicates the 2σ credibility upper limit on the average mass of UDGs derived from weak lensing Sifón et al. (2018). Finally, the vertical black dashed line corresponds to $N_{GC} = 1$.

As a means of comparison, we also do the same test for the population of GC-enriched UDGs from van Dokkum et al. (2017). While the two tests are not directly comparable since the sample of van Dokkum et al. (2017) was at least partially biased to select extreme objects (as in the cases of galaxies DF44 and DFX1), we find that their sample is not consistent with equation (6), with a *p*-value much less than 1 per cent.

Aside from DF44 and DFX1, the galaxies measured by van Dokkum et al. (2017) also include a list of 12 UDGs selected from the Yagi et al. (2016) catalogue of LSB galaxies that are also present in the Coma Cluster Treasury Program[4] footprint. Importantly, this should represent a small but unbiased sample of Coma UDGs. After selecting only these sources and repeating the test, we find that the Coma sample is still inconsistent with equation (6). This may indicate that UDGs in Coma have more GCs than galaxies in Fornax in the same luminosity range. We find that the choice in prior for the GC half-number radius does not impact this result; for a detailed discussion see Appendix D.

4.6 Effect of the GCLF

As stated in Section 3.4, we have adopted a Gaussian GCLF with a mean of $24m_g$ and standard deviation of $0.7m_g$. However, dwarf galaxies can have varied GCLFs and it is important to show that our results are robust against this. Villegas et al. (2010) have measured

[4]https://archive.stsci.edu/prepds/coma/

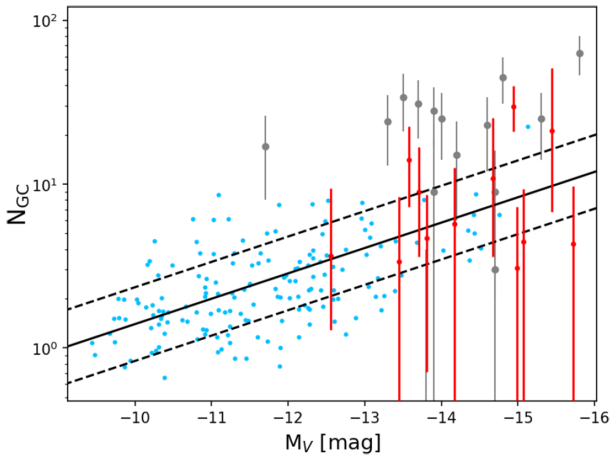

Figure 9. Power-law fit to N_{GC} versus M_V for our LSBG sample (solid black line) along with an estimate of the 1σ scatter (black dashed lines). Blue points: Our LSBG sample. Red error bars: Our UDG sample. Grey error bars: The sample of GC-enriched UDGs from van Dokkum et al. (2017).

the g-band GCLFs for 43 early-type galaxies in the Fornax cluster, down to galaxies with absolute B-band magnitudes of around −16. We use this catalogue as a means to test what would happen to our measurements if the GCLF was wider and has turnover magnitude fainter than our adopted value, i.e. to get an upper limit on the inferences on N_{GC}.

From the Villegas et al. (2010) catalogue, we measure a mean GCLF with mean $24 \pm 0.1 m_g$ and a standard deviation of $0.84 \pm 0.21 m_g$ after clipping outliers at 2σ. We note that we selected from their catalogue only galaxies with absolute B magnitudes fainter than −18 to target dwarf galaxies for this calculation. This suggests that the GCLF might be wider than what we have assumed previously. Integrating the RE over the 1σ deeper and wider GCLF and comparing to our previous estimates of the observed GC fraction, we find that the maximum correction in our N_{GC} is an increase of ∼20 per cent. We find that this is not sufficient to impact or change the overall results of our work (a 20 per cent increase in N_{GC} is sufficient to increase an M_{halo} estimate by ∼0.1dex).

4.7 Effect of nuclear star clusters

We do not treat potential NSCs any differently from GCs in our analysis; GCCs are defined by their magnitude and colour. While we have imposed a bright-end magnitude cut on our sample of GCCs, there is still potential for faint NSCs to contaminate our sample and therefore increase the number of GCCs for a target galaxy by one. For the galaxies with low estimates of N_{GC}, this can amount to a significant source of error. However, most of our target galaxies have $M_* \leq 10^8\,M_\odot$ and are thus expected to have a low nucleation fraction (between 0.7 at $10^8\,M_\odot$ and 0.0 at $10^5\,M_\odot$, as shown in fig. 8 of Sánchez-Janssen et al. 2018).

Removing GCCs close to the centres of galaxies introduces a subjective bias. However, we note that all the galaxies in our sample have already been visually classified as either nucleated or non-nucleated by Venhola et al. (2017). This number amounts to 10 per cent of the catalogue. After applying our bright-end magnitude cut, this leaves us with 13 galaxies that are potentially contaminated by an NSC. To quantify the effect this may have on our estimates of M_{halo}, we simply drop these sources from the sample and repeat the analysis. We find that the results do not change; the new binned-average estimates of M_{halo} are consistent within much less than 1σ with those displayed in Fig. 8.

5 DISCUSSION AND CONCLUSIONS

In this paper we have estimated the halo masses of a sample of 175 LSB galaxies in the Venhola et al. (2017) catalogue using the sizes of their GC populations, including a sub-sample of 12 UDGs. This constitutes the largest sample of low-mass galaxies so-far analysed for this kind of study. Candidate globular clusters were identified in the g band using measurements from the PROFOUND photometry package. We also applied a colour selection based on photometric measurements of a set of spectroscopically confirmed Fornax cluster GCs, using PSF-corrected aperture magnitudes measured in the u, g, r, i bands. Following this, we used a Bayesian Mixture model approach (influenced by the work of Amorisco et al. 2018) to infer the total number of GCs associated with each target galaxy, assuming a GCLF appropriate for our sample.

Our estimates of N_{GC} for the overall population are qualitatively consistent with more compact dwarf galaxies when plotted against M_V. We find that the sample of UDGs are statistically consistent with a power-law fit to the N_{GC} measurements for LSBGs, indicating that there is no discontinuity between the two populations; our sample of UDGs does not have a statistically significant excess of GCs compared to smaller LSB galaxies in the same luminosity range.

We converted the inferences on N_{GC} to M_{halo} using the empirical relation of Harris et al. (2017). We additionally derived stellar masses for the galaxies from the empirical relation of Taylor et al. (2011), using IMFIT galaxy models. Overall, the M_* estimates are consistent with dwarf galaxies and the M_{halo} estimates are consistent with dwarf sized haloes. The LSBG galaxy population appears consistent with the extrapolated Brook et al. (2014) abundance-matching relation between M_* and M_{halo} and as an extension of measurements from typical dwarf galaxies, but perhaps with slightly larger M_{halo} for the average dwarf at a given M_*. We suggest that this might be a systematic effect due to the environment; it is possible that only LSB galaxies with high M/L ratios are able to survive in the Fornax core. However, as Forbes et al. (2018) have shown, the M_{halo} estimates may be too large because of a breakdown in accuracy of the N_{GC}–M_{halo} relation in the low-mass regime, and it is not yet clear how this affects our estimates.

None of our UDGs have median values of N_{GC} above the empirical boundary marking GC-rich systems measured by Amorisco et al. (2018). However, 5 are consistent within their 1σ uncertainties. Several LSBGs also have potential for GC-richness, and 13 are at least 1σ above the required threshold. Such objects could make interesting sources for a follow-up study, given that they could represent a continuation of GC-rich objects down to very low stellar mass. If genuine, they could mean that enhanced GC systems are not unique to UDGs and the mechanisms by which UDGs are produced are separate from those by which LSB galaxies gain enriched GC systems, something also observed by Amorisco et al. (2018).

Using a weighted histogram approach, we have shown that the GC population of our target galaxies is predominantly blue compared to the overall GC population in Fornax. Our result is consistent with the blue peak in $(g - i)$ recorded by D'Abrusco et al. (2016), with a relative depletion of red GCs. Further still, the blue peak of our GC coincides with the $\pm 1\sigma$ range of the galaxy colours. There is tentative evidence in $(g - r)$ that the galaxies may be slightly redder than the GCs, but since this is not a significant effect we do not comment on this further.

The Coma cluster UDGs measured by van Dokkum et al. (2017) seem to have significantly more GCs than what we see in the Fornax cluster. It is notable that our sample is confined to the core of the Fornax cluster. While Lim et al. (2018) show that there is no particular trend of specific frequency S_N with cluster-centric radius for bright UDGs in Coma, they also show that S_N decreases with cluster-centric radius for fainter galaxies; if anything this could mean that we probe a population with systematically higher N_{GC} at a given M_* than in the cluster outskirts. Two possibilities are that GC-enriched UDGs are comparatively rare objects and we simply do not observe them because Fornax is much less massive than Coma, or the denser environment of the Coma cluster plays a positive role in UDG GC formation or acquisition. We suggest that future studies could provide complete measurements of N_{GC} for UDGs in other clusters (e.g. Virgo) to address this question.

Our measurements are sufficient to rule out the failed L_* formation theory for UDGs because the halo mass estimates indicate that they reside in dwarf sized haloes. We find a continuation in properties between UDGs and smaller LSBGs such that it does not seem that UDGs have a unique or special formation mechanism. Since few of our UDGs are convincingly GC-rich compared to those in Coma, we speculate that this property may be related to environmental density. Perhaps the Coma objects are more efficiently stripped of gas in the Coma core, thus forming fewer stars relative to their halo mass, resulting in systems that appear GC-rich for their stellar mass. A consequence of this effect is that the fraction of GC-rich UDGs should decline with cluster-centric radius, and this may be a valuable way to estimate the relative strengths of secular versus environmentally driven formation mechanisms.

ACKNOWLEDGEMENTS

We are grateful to Dr. Adriano Agnello for a helpful discussion on Bayesian mixture models.

We would also like to acknowledge helpful suggestions provided by Dr. Arianna Di Cintio.

We also thank the referee, Dr. Michael Beasley, for constructive comments.

CW is supported by the Deutsche Forschungsgemeinschaft (DFG, German Research Foundation) through project 394551440.

GvdV acknowledges funding from the European Research Council (ERC) under the European Union's Horizon 2020 research and innovation programme under grant agreement no. 724857 (Consolidator Grant ArcheoDyn).

AV would like to thank the Vilho, Yrjö, and Kalle Väisälä Foundation of the Finnish Academy of Science and Letters for the financial support.

RFP and AV acknowledge financial support from the European Union's Horizon 2020 research and innovation programme under the Marie Sklodovska-Curie grant agreement no. 721463 to the SUNDIAL ITN network.

REFERENCES

Amorisco N. C., Loeb A., 2016, MNRAS, 459, L51
Amorisco N. C., Monachesi A., Agnello A., White S. D. M., 2018, MNRAS, 475, 4235
Bassino L. P., Faifer F. R., Forte J. C., Dirsch B., Richtler T., Geisler D., Schuberth Y., 2006, A&A, 451, 789
Beasley M. A., Trujillo I., 2016, ApJ, 830, 23
Beasley M. A., Romanowsky A. J., Pota V., Navarro I. M., Martinez Delgado D., Neyer F., Deich A. L., 2016, ApJ, 819, L20
Behroozi P. S., Wechsler R. H., Conroy C., 2013, ApJ, 770, 57
Blakeslee J. P. et al., 2009, ApJ, 694, 556
Bothun G. D., Impey C. D., Malin D. F., Mould J. R., 1987, AJ, 94, 23
Brook C. B., Di Cintio A., Knebe A., Gottlöber S., Hoffman Y., Yepes G., Garrison-Kimmel S., 2014, ApJ, 784, L14
Capaccioli M. et al., 2012, Science from the Next Generation Imaging and Spectroscopic Surveys. p. 1
Capaccioli M. et al., 2015, A&A, 581, A10
Carleton T., Errani R., Cooper M., Kaplinghat M., Peñarrubia J., 2018, preprint (arXiv:1805.06896)
Collins M. L. M. et al., 2013, ApJ, 768, 172
Conselice C. J., 2018, Res. Notes Am. Astron. Soc., 2, 43
Conselice C. J., Gallagher J. S., III, Wyse R. F. G., 2003, AJ, 125, 66
D'Abrusco R. et al., 2016, ApJ, 819, L31
Dalcanton J. J., Spergel D. N., Summers F., 1995, preprint (arXiv: Astrophysics e-prints)
Davies J. I., Davies L. J. M., Keenan O. C., 2016, MNRAS, 456, 1607
Di Cintio A., Brook C. B., Dutton A. A., Macciò A. V., Obreja A., Dekel A., 2017, MNRAS, 466, L1
Disney M. J., 1976, Nature, 263, 573
Drinkwater M. J., Gregg M. D., Colless M., 2001, ApJ, 548, L139
Driver S. P. et al., 2011, MNRAS, 413, 971
Errani R., Peñarrubia J., Walker M. G., 2018, MNRAS, 481, 5073
Erwin P., 2015, ApJ, 799, 226
Ester M., Kriegel H.-P., Sander J., Xu X., 1996, AAAI Press, p. 226
Ferguson H. C., 1989, Ap&SS, 157, 227
Forbes D. A., 2017, MNRAS, 472, L104
Forbes D. A., Read J. I., Gieles M., Collins M. L. M., 2018, MNRAS, 481, 5592
Georgiev I. Y., Puzia T. H., Goudfrooij P., Hilker M., 2010, MNRAS, 406, 1967
Grado A., Capaccioli M., Limatola L., Getman F., 2012, Mem. Soc. Astron. Ital. Suppl., 19, 362
Harris W. E., Harris G. L. H., Alessi M., 2013, ApJ, 772, 82
Harris W. E., Blakeslee J. P., Harris G. L. H., 2017, ApJ, 836, 67
Henden A. A., Levine S. E., Terrell D., Smith T. C., Welch D., 2012, J. Am. Assoc. Var. Star Obs., 40, 430
Hudson M. J., Robison B., 2018, MNRAS, 477, 3869
Hudson M. J., Harris G. L., Harris W. E., 2014, ApJ, 787, L5
Hughes J. P., 1998, in Mazure A., Casoli F., Durret F., Gerbal D., eds, Untangling Coma Berenices: A New Vision of an Old Cluster
Impey C., Bothun G., Malin D., 1988, ApJ, 330, 634
Iodice E. et al., 2016, ApJ, 820, 42
Jester S. et al., 2005, AJ, 130, 873
Jiang F., Dekel A., Freundlich J., Romanowsky A. J., Dutton A., Maccio A., Di Cintio A., 2018, preprint (arXiv:e-prints)
Jimenez R., Padoan P., Matteucci F., Heavens A. F., 1998, MNRAS, 299, 123
Jordán A. et al., 2007, ApJS, 169, 213
Koda J., Yagi M., Yamanoi H., Komiyama Y., 2015, ApJ, 807, L2
Kuijken K., 2011, The Messenger, 146, 8
Laporte C. F. P., Agnello A., Navarro J. F., 2018, MNRAS, 484, 245
Lim S., Peng E. W., Côté P., Sales L. V., den Brok M., Blakeslee J. P., Guhathakurta P., 2018, ApJ, 862, 82
Mancera Piña P. E., Peletier R. F., Aguerri J. A. L., Venhola A., Trager S., Choque Challapa N., 2018, MNRAS, 481, 4381
Mastropietro C., Moore B., Mayer L., Debattista V. P., Piffaretti R., Stadel J., 2005, MNRAS, 364, 607
McFarland J. P., Verdoes-Kleijn G., Sikkema G., Helmich E. M., Boxhoorn D. R., Valentijn E. A., 2011, preprint (arXiv:1110.2509)
McGaugh S. S., 1996, MNRAS, 280, 337
Mihos J. C. et al., 2015, ApJ, 809, L21

Miller B. W., Lotz J. M., 2007, ApJ, 670, 1074
Moore B., Lake G., Katz N., 1998, ApJ, 495, 139
Moster B. P., Somerville R. S., Maulbetsch C., van den Bosch F. C., Macciò A. V., Naab T., Oser L., 2010, ApJ, 710, 903
Mowla L., van Dokkum P., Merritt A., Abraham R., Yagi M., Koda J., 2017, ApJ, 851, 27
Muñoz R. P. et al., 2015, ApJ, 813, L15
Peng E. W. et al., 2006, ApJ, 639, 95
Peng C. Y., Ho L. C., Impey C. D., Rix H.-W., 2002, AJ, 124, 266
Pota V. et al., 2018, MNRAS, 481, 1744
Prole D. J., Davies J. I., Keenan O. C., Davies L. J. M., 2018, MNRAS, 478, 667
Rejkuba M., 2012, Ap&SS, 341, 195
Robotham A. S. G., Davies L. J. M., Driver S. P., Koushan S., Taranu D. S., Casura S., Liske J., 2018, MNRAS, 476, 3137
Román J., Trujillo I., 2017, MNRAS, 468, 703
Rong Y., Guo Q., Gao L., Liao S., Xie L., Puzia T. H., Sun S., Pan J., 2017, MNRAS, 470, 4231
Sabatini S., Davies J., Scaramella R., Smith R., Baes M., Linder S. M., Roberts S., Testa V., 2003, MNRAS, 341, 981
Sánchez-Janssen R. et al., 2018, preprint (arXiv: e-prints)
Sandage A., Binggeli B., 1984, AJ, 89, 919
Schuberth Y., Richtler T., Hilker M., Dirsch B., Bassino L. P., Romanowsky A. J., Infante L., 2010, A&A, 513, A52
Sifón C., van der Burg R. F. J., Hoekstra H., Muzzin A., Herbonnet R., 2018, MNRAS, 473, 3747
Spitler L. R., Forbes D. A., 2009, MNRAS, 392, L1
Taylor E. N. et al., 2011, MNRAS, 418, 1587
Toloba E. et al., 2018, ApJ, 856, L31
Trujillo I. et al., 2018, preprint (arXiv:1806.10141)
van der Burg R. F. J., Muzzin A., Hoekstra H., 2016, A&A, 590, A20
van der Burg R. F. J. et al., 2017, A&A, 607, A79
van Dokkum P. G., Abraham R., Merritt A., Zhang J., Geha M., Conroy C., 2015, ApJ, 798, L45
van Dokkum P. et al., 2016, ApJ, 828, L6
van Dokkum P. et al., 2017, ApJ, 844, L11
van Dokkum P. et al., 2018, Nature, 555, 629
Venhola A. et al., 2017, A&A, 608, A142(V17)
Villegas D. et al., 2010, ApJ, 717, 603
Wittmann C., Lisker T., Pasquali A., Hilker M., Grebel E. K., 2016, MNRAS, 459, 4450
Wittmann C. et al., 2017, MNRAS, 470, 1512
Wolf C. et al., 2018, Publ. Astron. Soc. Aust., 35, e010
Yagi M., Koda J., Komiyama Y., Yamanoi H., 2016, ApJS, 225, 11
Yozin C., Bekki K., 2015, MNRAS, 452, 937

APPENDIX A: GALAXY MODELLING

We used IMFIT to fit single Sérsic profiles to each target galaxy. Fortunately, Venhola et al. (2017) (hereafter V17) already provide such fits in the *r* band. While here we choose to remeasure the profiles for consistency with the other bands, we do make use of these data as initial guesses in the fitting. Our approach was to iteratively fit the galaxy in the *r* band, each time improving the mask of pixels to ignore in the fit. The general procedure for a galaxy is as follows:

(i) Obtain an $8 \times 8r^{r}_{\mathrm{e,V17}}$ *r*-band cut-out.
(ii) Subtract the V17 model from the result (include nuclear PSF if indicated by V17).
(iii) Use DEEPSCAN[5] (Prole et al. 2018) to get sky and RMS estimates from the result.

[5]https://github.com/danjampro/DeepScan

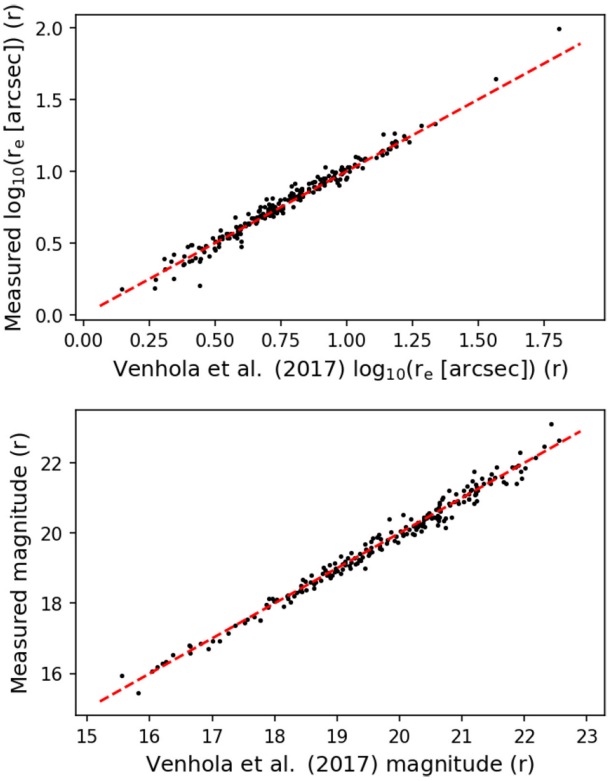

Figure A1. Our galaxy measurements (IMFIT) versus those of V17 (GALFIT). Red dashed line: The one-to-one relation. The RMS of the residuals are 0.18 mag and 0.04 dex in r_e.

(iv) Create a smoothed image by applying a Gaussian filter with RMS = 2 pixels.
(v) Mask all pixels with $\geq 6\sigma$ significance on the smoothed image.
(vi) Use IMFIT to fit a Sérsic model to the original data with the sky subtracted, ignoring pixels in the mask.
(vii) Repeat steps 2–6 three times, each time updating the model image and mask.
(viii) Repeat steps 1, 3, and 6 for the other bands, using the same *r*-band mask in each.

For the DEEPSCAN sky estimates we used a mesh size equal to the image size and performed three masking iterations. If the galaxy was indicated as nucleated by V17, we also fit a Moffat profile simultaneously with the Sérsic model. We found that in a minority of cases the residuals from the V17 fits were quite large, such that we had to modify the masks manually.

In the case of FDS11_LSB2, the largest galaxy in our sample (with $r^{r}_{\mathrm{e,V17}} = 76$ arcsec), we re-binned the data by a factor of 5 to make the fit easier (the original fitting region was $\sim$3000 $\times$ 3000 pixels). Over this region the sky background level varies significantly, so we modified the DEEPSCAN sky modelling to use mesh sizes of $\sim$200 arcsec and median filtered in 3 $\times$ 3 meshes. We note that an image of FDS11_LSB2 is displayed in fig. 20 of V17.

Overall our results are consistent with V17 (Fig. A1), with a few exceptions. These include FDS11_LSB2, which we measure to be 1.5 times larger than originally reported. This result was robust against changes in the size of the background mesh. We also note that we measure a slightly lower Sérsic index *n* for this object, and *n* is generally anticorrelated with r_e. This discrepancy likely arises from the difficulty involved in measuring such a large, diffuse

galaxy in a reasonably crowded field with a varying sky; we use `DeepScan` whereas V17 fit a 2D sky plane in their GALFIT (Peng et al. 2002) modelling. We also note that V17 did not leave the central coordinate of their model profiles as a free parameter.

Finally, we note that we were not able to obtain stable IMFIT models for several sources because they were too faint: FDS12_LSB42, FDS12_LSB47, FDS11_LSB16, and FDS12_LSB34. We therefore adopted the fits of V17 for these sources. Since V17 did not measure $(g-i)$ colours, we have omitted them from stellar mass calculations and from Fig. 8.

APPENDIX B: PHOTOMETRIC CALIBRATION

Starting from the VST tube-reduced data, we used PROFOUND to detect and select point sources. We additionally measured fixed-aperture magnitudes for each source with an estimate of that magnitude. These aperture magnitudes had to be corrected for both the limited size of the aperture with respect to the PSF in each band, but also the absolute calibration to AB magnitudes.

While there is no ideal set of standard stars in our footprint with which to calibrate the photometry, Cantiello et al. (in preparation) have used a set of existing, overlapping calibrated catalogues [ACSFCS (Jordán et al. 2007); APASS (Henden et al. 2012); SkyMapper (Wolf et al. 2018)] to calibrate their photometry in the same data. We have calibrated our own aperture magnitudes by matching our catalogue with theirs, selecting point sources as in Section 3.2 and applying a multiplicative correction to our measurements to nullify the mean offset between the measurement pairs. The RMS between our corrected aperture magnitudes with theirs is ∼0.05 mag in g, r, i and ∼0.2 mag in the shallower u band, for all matching point sources with corrected g magnitudes brighter than 23 mag.

During the calibration it was noticed that the reference catalogue of Cantiello et al. (in preparation) contained minor systematic offsets in the stellar locus between individual FDS frames, suggesting a systematic error in the absolute calibration. We have dealt with this by shifting each locus to a common position in colour–colour space. The net result of this is a maximum systematic uncertainty of ∼±0.05 mag in each colour plane. Finally, we note that since there is currently no available reference catalogue for FDS frame 12 we calibrated the photometry for that frame in accordance with FDS frame 11. This calibration is accurate enough to have negligible effects on our results.

APPENDIX C: COMPARISON WITH MILLER & LOTZ (2007)

As several of the sources in the Venhola et al. (2017) catalogue were also identified in the Fornax cluster catalogue (Ferguson 1989), we were encouraged to search for matches in the catalogue of dwarf ellipticals studied by Miller & Lotz (2007), who used the *HST* WFPC2 Dwarf Elliptical Galaxy Snapshot Survey to measure the GC populations for a sample of 69 galaxies. They measured $N_{\rm GC}$ using apertures of five times the exponential scale size of the galaxies, which roughly equates to $3r_e$ for a Sérsic index $n = 1$.

We find seven matches: FDS16_LSB33 (FCC0146), FDS12_LSB10 (FCC0238), FDS12_LSB4 (FCC0246), FDS11_LSB62 (FCC0254), FDS16_LSB58 (FCC0110), FDS16_LSB32 (FCC0144), and FDS12_LSB30 (FCC0212). Overall our results are reasonably consistent (albeit with large error bars), as is shown in Fig. C1. Note that in the figure one of the sources is not visible because it overlaps with another.

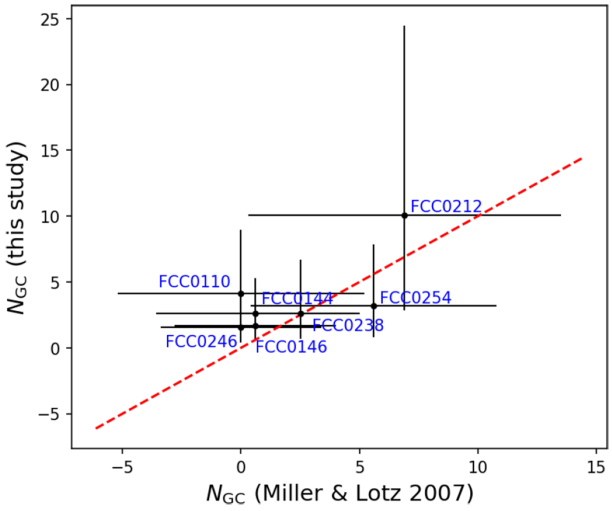

Figure C1. Comparison of GC number counts. The black points are median values from the MCMC posterior. The error bars span the range of 1σ. The red dashed line is the one-to-one relation. A chi-square test (accounting for the errors) shows that the null hypothesis that the measurements are consistent with the one-to-one relation cannot be rejected with confidence greater than around 4 per cent.

APPENDIX D: CHOICE OF PRIOR

While the choice for the prior on the GC half-number radius $r_{\rm h}$ is justified from previous literature measurements (van Dokkum et al. 2017; Amorisco et al. 2018; Lim et al. 2018), it is important to show how different choices may affect the results. This is particularly relevant because the spatial distributions of GCs for UDGs is not well known. By running the MCMC using different priors, we show in Fig. D1 that, despite the choice of prior in $r_{\rm h}$ strongly influencing the $r_{\rm h}$ posterior, the estimates of $N_{\rm GC}$ are robust.

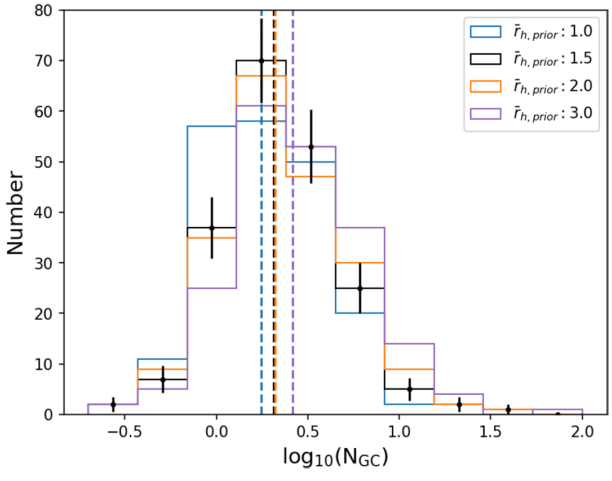

Figure D1. The distribution of $N_{\rm GC}$ estimates for our sample of galaxies as a function on the mean of the prior on the GC half-number radius, $\bar{r}_{\rm h,prior}$, in units of galaxy half-light radius. Also shown are the median values (dashed lines). Our value of $\bar{r}_{\rm h,prior} = 1.5r_{\rm e}$ is adopted from the literature and Poisson error bars are shown for this value.

A small increase in the mean of the prior on the GC half-number radius, $\bar{r}_{\rm h,prior}$, is not sufficient to significantly impact our results. However, more dramatic modifications may produce a more pronounced change. In general, lowering $\bar{r}_{\rm h,prior}$ increases the number of GC-poor systems, while increasing it results in more GC rich systems. However, the median value for the overall population is not significantly altered by using different priors. We finally note that repeating the analysis from Section 4.5 with $\bar{r}_{\rm h,prior} = 3r_{\rm e}$ leads us to the same conclusions; the overall result is robust against changes in the prior.

APPENDIX E: MEASUREMENTS TABLE

Table E1. Results of our analysis. Values enclosed in braces are 10th, 50th, and 90th percentiles from the MCMC posterior. Fiducial errors on M_V and $M_*/{\rm M}_\odot$ are ∼0.2 mag and 0.3 dex, respectively. For $r_{\rm e,r}$ the uncertainty is approximately 10 per cent of the value after measuring the scatter between our measurements and those of Venhola et al. (2017). We remind the readers that the estimates of $M_{\rm halo}$ should be considered as upper limits.

Target	M_V (mag)	$r_{\rm e,r}$ (kpc)	$\log_{10}(M_*\,[{\rm M}_\odot])$	$r_{\rm h}$ ($r_{\rm e,r}$)	$N_{\rm GC}$	$\log_{10}(M_{\rm halo}\,[{\rm M}_\odot])$
FDS10_LSB2	−11.0	0.46	6.3	{1.06, 2.04, 2.94}	{0.7, 3.7, 9.4}	{9.5, 10.3, 10.7}
FDS10_LSB3	−9.8	0.64	6.3	{0.57, 1.39, 2.40}	{0.4, 2.0, 4.9}	{9.2, 10.0, 10.4}
FDS10_LSB4	−11.7	0.39	6.5	{0.69, 1.65, 2.66}	{0.2, 1.1, 3.5}	{8.7, 9.7, 10.2}
FDS10_LSB5	−11.1	0.94	5.6	{1.35, 2.28, 3.27}	{2.2, 8.6, 19.6}	{10.0, 10.7, 11.1}
FDS10_LSB6	−10.4	0.30	5.8	{0.77, 1.75, 2.79}	{0.3, 1.4, 3.4}	{9.0, 9.8, 10.2}
FDS10_LSB8	−11.3	0.69	6.3	{0.78, 1.73, 2.73}	{0.3, 2.0, 6.2}	{9.1, 10.0, 10.5}
FDS10_LSB9	−9.9	0.35	5.8	{0.66, 1.37, 2.36}	{0.5, 2.0, 4.6}	{9.3, 10.0, 10.4}
FDS10_LSB10	−11.3	0.62	6.2	{0.64, 1.60, 2.65}	{0.1, 0.9, 2.9}	{8.6, 9.6, 10.1}
FDS10_LSB13	−10.2	0.40	5.9	{0.72, 1.51, 2.52}	{0.4, 1.8, 4.5}	{9.2, 9.9, 10.4}
FDS10_LSB14	−11.1	0.50	5.6	{0.71, 1.69, 2.69}	{0.2, 1.2, 3.6}	{8.9, 9.7, 10.2}
FDS10_LSB15	−11.3	0.53	6.5	{0.43, 1.18, 2.27}	{0.5, 2.2, 5.0}	{9.3, 10.0, 10.4}
FDS10_LSB16	−10.6	0.34	6.1	{0.79, 1.62, 2.54}	{0.3, 1.5, 3.6}	{9.0, 9.8, 10.2}
FDS10_LSB23	−12.6	0.78	6.7	{0.92, 1.91, 2.94}	{0.4, 2.3, 7.2}	{9.1, 10.0, 10.6}
FDS10_LSB25	−14.2	2.06	7.6	{0.85, 1.80, 2.81}	{1.0, 5.7, 15.9}	{9.6, 10.5, 11.0}
FDS10_LSB29	−13.4	0.85	7.1	{0.74, 1.64, 2.61}	{0.4, 2.2, 6.5}	{9.1, 10.0, 10.5}
FDS10_LSB35	−12.3	0.35	6.6	{0.74, 1.70, 2.65}	{0.2, 1.4, 4.0}	{8.9, 9.8, 10.3}
FDS10_LSB38	−12.0	0.78	6.5	{0.19, 1.05, 2.15}	{0.8, 2.8, 6.7}	{9.5, 10.1, 10.5}
FDS10_LSB40	−11.0	0.90	6.1	{1.19, 1.92, 2.73}	{2.1, 6.1, 11.9}	{10.0, 10.5, 10.8}
FDS10_LSB41	−12.3	0.63	6.8	{0.73, 1.64, 2.64}	{0.4, 2.3, 7.8}	{9.1, 10.0, 10.6}
FDS10_LSB43	−11.1	0.51	6.2	{0.71, 1.72, 2.71}	{0.1, 0.9, 3.6}	{8.7, 9.6, 10.2}
FDS10_LSB44	−11.1	0.31	6.3	{0.30, 0.95, 2.15}	{0.5, 1.7, 3.7}	{9.3, 9.9, 10.3}
FDS10_LSB45	−12.1	0.53	6.7	{0.85, 1.84, 2.80}	{0.3, 1.7, 5.6}	{9.0, 9.9, 10.5}
FDS10_LSB46	−10.7	0.29	5.9	{0.66, 1.58, 2.63}	{0.2, 1.4, 4.5}	{8.8, 9.8, 10.3}
FDS10_LSB49	−12.3	0.55	6.8	{0.81, 1.74, 2.79}	{0.3, 1.7, 5.3}	{9.0, 9.9, 10.4}
FDS10_LSB51	−12.1	0.80	6.8	{0.91, 1.81, 2.79}	{0.4, 2.6, 7.2}	{9.2, 10.1, 10.6}
FDS10_LSB52	−13.8	1.54	7.4	{0.41, 1.12, 2.36}	{1.3, 4.7, 10.5}	{9.8, 10.4, 10.8}
FDS10_LSB53	−11.5	0.57	6.5	{0.52, 1.25, 2.31}	{0.4, 1.8, 4.6}	{9.2, 9.9, 10.4}
FDS10_LSB54	−9.7	0.33	6.7	{0.96, 1.82, 2.66}	{0.3, 1.2, 2.6}	{9.0, 9.7, 10.1}
FDS10_LSB55	−12.4	0.55	7.0	{0.88, 1.77, 2.75}	{1.2, 5.0, 11.4}	{9.7, 10.4, 10.8}
FDS10_LSB56	−9.7	0.47	5.4	{0.68, 1.62, 2.65}	{0.2, 1.1, 3.2}	{8.7, 9.7, 10.2}
FDS11_LSB4	−11.2	0.46	5.9	{0.70, 1.77, 2.72}	{0.3, 1.7, 5.5}	{9.0, 9.9, 10.4}
FDS11_LSB6	−10.3	0.63	6.6	{0.53, 1.31, 2.33}	{0.5, 2.0, 5.0}	{9.3, 10.0, 10.4}
FDS11_LSB7	−10.8	0.76	7.7	{1.26, 2.05, 2.92}	{1.6, 6.1, 13.9}	{9.8, 10.5, 10.9}
FDS11_LSB8	−10.3	0.48	6.2	{0.76, 1.71, 2.70}	{0.2, 1.5, 4.5}	{8.9, 9.8, 10.3}
FDS11_LSB10	−11.9	0.81	6.5	{0.53, 1.38, 2.44}	{0.5, 2.1, 5.0}	{9.2, 10.0, 10.4}
FDS11_LSB11	−10.9	0.56	6.3	{0.96, 1.86, 2.76}	{0.4, 2.6, 7.2}	{9.2, 10.1, 10.6}
FDS11_LSB13	−11.1	0.48	6.3	{0.96, 1.97, 2.93}	{0.3, 2.2, 6.3}	{9.0, 10.0, 10.5}
FDS11_LSB14	−11.8	1.07	7.3	{0.84, 1.82, 2.78}	{0.3, 2.3, 7.1}	{9.1, 10.0, 10.6}
FDS11_LSB15	−12.3	0.71	7.3	{0.79, 1.69, 2.65}	{0.7, 3.9, 11.4}	{9.5, 10.3, 10.8}
FDS11_LSB16	−12.5	1.50	–	{0.88, 1.79, 2.75}	{0.7, 3.6, 12.0}	{9.4, 10.2, 10.8}
FDS11_LSB18	−10.9	0.61	5.6	{0.08, 0.44, 1.94}	{0.6, 2.2, 5.1}	{9.4, 10.0, 10.4}
FDS11_LSB30	−13.7	1.75	7.4	{1.12, 1.92, 2.79}	{2.2, 8.9, 20.3}	{10.0, 10.7, 11.1}
FDS11_LSB35	−11.3	0.69	6.0	{0.73, 1.45, 2.43}	{0.9, 3.8, 8.4}	{9.6, 10.3, 10.7}
FDS11_LSB36	−10.9	0.79	6.1	{0.74, 1.58, 2.54}	{0.4, 2.3, 6.7}	{9.1, 10.0, 10.5}
FDS11_LSB38	−14.9	1.56	8.0	{0.69, 1.05, 1.53}	{18.0, 29.8, 43.7}	{11.0, 11.3, 11.5}
FDS11_LSB39	−10.2	0.38	5.0	{0.86, 1.74, 2.71}	{0.8, 3.2, 7.3}	{9.5, 10.2, 10.6}
FDS11_LSB40	−9.5	0.38	4.5	{0.65, 1.66, 2.75}	{0.2, 0.9, 2.8}	{8.7, 9.6, 10.1}
FDS11_LSB41	−13.0	0.97	7.0	{0.91, 1.82, 2.82}	{0.4, 2.4, 7.8}	{9.1, 10.0, 10.6}
FDS11_LSB42	−12.1	1.22	6.5	{0.66, 1.65, 2.73}	{0.5, 3.1, 8.8}	{9.3, 10.2, 10.7}
FDS11_LSB43	−9.8	0.42	5.6	{0.84, 1.84, 2.88}	{0.2, 1.5, 4.9}	{8.8, 9.8, 10.4}
FDS11_LSB44	−10.0	0.44	5.7	{0.86, 1.78, 2.74}	{0.3, 1.9, 5.3}	{9.0, 9.9, 10.4}
FDS11_LSB45	−11.4	0.71	6.3	{0.71, 1.78, 2.74}	{0.2, 1.5, 4.9}	{8.8, 9.8, 10.4}

Table E1 – *continued*

Target	M_V (mag)	$r_{e,r}$ (kpc)	$\log_{10}(M_* [M_\odot])$	r_h ($r_{e,r}$)	N_{GC}	$\log_{10}(M_{halo} [M_\odot])$
FDS11_LSB46	−10.9	0.74	6.0	{0.78, 1.72, 2.64}	{0.2, 1.3, 4.7}	{8.7, 9.7, 10.4}
FDS11_LSB47	−13.0	1.05	7.0	{0.37, 1.42, 2.38}	{2.5, 7.7, 17.1}	{10.1, 10.6, 11.0}
FDS11_LSB49	−13.7	1.34	7.4	{0.16, 0.71, 2.32}	{1.4, 4.4, 10.2}	{9.8, 10.3, 10.8}
FDS11_LSB51	−10.3	0.84	6.5	{0.82, 1.56, 2.52}	{0.7, 2.8, 6.1}	{9.4, 10.1, 10.5}
FDS11_LSB53	−10.8	0.33	6.0	{1.13, 1.91, 2.78}	{1.1, 3.8, 7.5}	{9.7, 10.3, 10.6}
FDS11_LSB55	−11.4	0.89	6.0	{0.84, 1.78, 2.77}	{0.3, 2.3, 7.1}	{9.1, 10.0, 10.6}
FDS11_LSB56	−11.2	0.53	6.1	{0.62, 1.59, 2.65}	{0.2, 1.1, 3.4}	{8.8, 9.7, 10.2}
FDS11_LSB57	−12.3	0.65	6.8	{0.62, 1.77, 2.71}	{2.3, 7.5, 16.1}	{10.0, 10.6, 11.0}
FDS11_LSB58	−11.2	0.90	5.9	{0.38, 1.72, 2.79}	{1.6, 6.1, 14.4}	{9.8, 10.5, 10.9}
FDS11_LSB59	−13.0	0.85	7.1	{0.34, 1.43, 2.63}	{0.8, 3.7, 10.1}	{9.5, 10.3, 10.7}
FDS11_LSB60	−13.8	1.21	7.4	{0.43, 0.93, 1.89}	{3.6, 8.0, 15.0}	{10.2, 10.6, 10.9}
FDS11_LSB61	−11.9	0.61	6.6	{0.90, 1.73, 2.71}	{0.5, 2.7, 7.2}	{9.3, 10.1, 10.6}
FDS11_LSB62	−14.4	1.21	7.7	{0.91, 1.83, 2.72}	{0.5, 3.4, 10.4}	{9.3, 10.2, 10.8}
FDS11_LSB63	−10.9	0.50	6.0	{0.94, 1.82, 2.71}	{0.4, 2.1, 5.1}	{9.2, 10.0, 10.4}
FDS11_LSB64	−10.8	0.30	6.2	{0.85, 1.73, 2.67}	{0.3, 1.7, 4.0}	{9.1, 9.9, 10.3}
FDS11_LSB65	−12.5	0.81	6.7	{1.22, 2.09, 2.92}	{2.6, 8.0, 16.2}	{10.1, 10.6, 11.0}
FDS11_LSB66	−10.9	0.55	6.3	{0.65, 1.65, 2.68}	{0.2, 1.3, 4.0}	{8.8, 9.7, 10.3}
FDS11_LSB67	−11.7	0.55	6.4	{1.09, 2.00, 2.97}	{1.1, 5.0, 11.8}	{9.7, 10.4, 10.8}
FDS11_LSB68	−12.3	0.73	6.4	{0.79, 1.68, 2.69}	{0.7, 3.7, 9.7}	{9.5, 10.3, 10.7}
FDS11_LSB69	−12.9	1.29	6.9	{0.67, 1.67, 2.65}	{1.6, 6.2, 14.9}	{9.8, 10.5, 10.9}
FDS11_LSB71	−11.6	0.55	6.0	{0.65, 1.72, 2.76}	{0.2, 1.2, 4.0}	{8.8, 9.7, 10.3}
FDS11_LSB72	−11.9	0.81	6.5	{0.60, 1.45, 2.52}	{0.4, 2.0, 5.3}	{9.2, 10.0, 10.4}
FDS11_LSB73	−10.3	0.33	5.1	{0.82, 1.76, 2.76}	{0.3, 1.7, 4.9}	{9.0, 9.9, 10.4}
FDS11_LSB74	−14.0	0.97	7.3	{0.60, 1.42, 2.51}	{0.8, 4.0, 10.0}	{9.5, 10.3, 10.7}
FDS11_LSB76	−10.2	0.50	5.9	{0.70, 1.73, 2.80}	{0.2, 1.3, 4.1}	{8.8, 9.8, 10.3}
FDS11_LSB77	−12.7	0.49	7.0	{0.68, 1.65, 2.61}	{0.2, 1.2, 3.9}	{8.7, 9.7, 10.3}
FDS11_LSB78	−14.3	1.19	7.6	{0.97, 1.93, 2.88}	{1.0, 5.2, 13.8}	{9.6, 10.4, 10.9}
FDS11_LSB79	−12.4	0.52	6.8	{0.29, 1.27, 2.48}	{0.6, 2.3, 5.4}	{9.3, 10.0, 10.4}
FDS11_LSB80	−12.6	0.62	6.8	{0.79, 1.66, 2.65}	{0.3, 2.0, 5.6}	{9.0, 10.0, 10.5}
FDS11_LSB81	−13.1	0.78	7.1	{0.44, 1.35, 2.31}	{2.0, 5.8, 11.7}	{10.0, 10.5, 10.8}
FDS12_LSB3	−13.4	1.63	7.3	{0.88, 1.86, 2.81}	{0.5, 3.4, 11.1}	{9.2, 10.2, 10.8}
FDS12_LSB4	−13.2	0.99	7.0	{0.77, 1.80, 2.77}	{0.2, 1.7, 5.7}	{8.9, 9.9, 10.5}
FDS12_LSB5	−9.9	0.47	5.0	{0.72, 1.84, 2.86}	{0.2, 1.5, 4.9}	{8.9, 9.8, 10.4}
FDS12_LSB6	−9.4	0.42	5.1	{0.74, 1.67, 2.61}	{0.2, 1.1, 3.3}	{8.7, 9.7, 10.2}
FDS12_LSB8	−10.5	0.33	4.1	{1.01, 1.84, 2.68}	{0.9, 3.2, 6.6}	{9.6, 10.2, 10.5}
FDS12_LSB9	−13.4	0.99	6.8	{0.97, 1.91, 2.79}	{0.8, 4.5, 12.8}	{9.5, 10.4, 10.9}
FDS12_LSB10	−13.5	1.03	6.8	{0.89, 1.83, 2.80}	{0.4, 2.8, 9.1}	{9.2, 10.1, 10.7}
FDS12_LSB11	−12.1	0.65	6.5	{0.89, 1.89, 2.86}	{0.3, 2.1, 6.1}	{9.1, 10.0, 10.5}
FDS12_LSB12	−12.1	0.93	5.9	{0.92, 1.84, 2.78}	{0.5, 3.4, 9.7}	{9.3, 10.2, 10.7}
FDS12_LSB13	−13.1	1.31	6.8	{0.98, 1.96, 2.88}	{0.7, 4.7, 14.5}	{9.4, 10.4, 10.9}
FDS12_LSB14	−10.3	0.33	5.7	{0.65, 1.60, 2.63}	{0.2, 1.0, 3.2}	{8.7, 9.6, 10.2}
FDS12_LSB16	−11.5	0.73	6.1	{0.96, 1.85, 2.75}	{0.4, 2.4, 7.3}	{9.2, 10.0, 10.6}
FDS12_LSB17	−11.4	0.53	6.1	{0.79, 1.77, 2.81}	{0.2, 1.6, 5.2}	{8.9, 9.9, 10.4}
FDS12_LSB19	−10.2	0.36	5.4	{0.79, 1.77, 2.80}	{0.3, 1.6, 4.7}	{9.0, 9.8, 10.4}
FDS12_LSB20	−11.8	0.49	6.5	{1.03, 2.00, 2.91}	{1.0, 5.2, 12.2}	{9.6, 10.4, 10.8}
FDS12_LSB21	−12.5	0.54	6.7	{0.96, 1.81, 2.74}	{1.8, 6.0, 12.7}	{9.9, 10.5, 10.9}
FDS12_LSB22	−12.9	0.75	6.7	{0.75, 1.80, 2.83}	{0.2, 1.5, 5.4}	{8.9, 9.8, 10.4}
FDS12_LSB23	−11.2	0.50	6.0	{0.53, 1.38, 2.45}	{0.3, 1.7, 4.5}	{9.1, 9.9, 10.4}
FDS12_LSB24	−10.4	0.53	6.8	{0.76, 1.74, 2.74}	{0.2, 1.6, 5.6}	{8.9, 9.9, 10.5}
FDS12_LSB25	−9.7	0.32	3.5	{0.97, 1.87, 2.84}	{0.3, 1.5, 4.4}	{9.0, 9.8, 10.3}
FDS12_LSB26	−12.3	0.48	6.3	{0.19, 0.91, 2.20}	{0.5, 2.3, 5.4}	{9.3, 10.0, 10.4}
FDS12_LSB28	−12.3	0.49	6.0	{0.57, 1.41, 2.52}	{0.8, 3.5, 9.4}	{9.5, 10.2, 10.7}
FDS12_LSB29	−13.0	0.81	6.6	{0.80, 1.68, 2.67}	{1.2, 5.3, 12.6}	{9.7, 10.4, 10.9}
FDS12_LSB30	−14.7	2.00	7.7	{1.18, 2.22, 3.18}	{2.0, 10.9, 32.2}	{10.0, 10.8, 11.3}
FDS12_LSB31	−10.2	0.42	5.4	{1.11, 1.96, 2.86}	{0.7, 3.4, 8.4}	{9.4, 10.2, 10.7}
FDS12_LSB32	−10.7	0.42	5.6	{0.81, 1.81, 2.79}	{0.3, 1.8, 5.1}	{9.0, 9.9, 10.4}
FDS12_LSB33	−11.2	0.61	6.1	{0.72, 1.68, 2.70}	{0.2, 1.2, 4.1}	{8.8, 9.7, 10.3}
FDS12_LSB34	−11.9	1.44	–	{1.25, 2.07, 2.94}	{1.3, 7.5, 20.3}	{9.7, 10.6, 11.1}
FDS12_LSB35	−11.5	0.42	6.1	{0.90, 1.73, 2.65}	{0.2, 1.5, 5.3}	{8.8, 9.8, 10.4}
FDS12_LSB42	−14.5	1.25	–	{0.87, 1.83, 2.82}	{0.7, 4.1, 11.9}	{9.4, 10.3, 10.8}
FDS12_LSB46	−11.1	0.34	5.9	{0.70, 1.72, 2.69}	{0.2, 1.0, 3.4}	{8.7, 9.6, 10.2}
FDS12_LSB47	−10.4	0.39	–	{0.91, 1.89, 2.87}	{0.3, 1.7, 4.8}	{9.0, 9.9, 10.4}

Table E1 *– continued*

Target	M_V (mag)	$r_{e,r}$ (kpc)	$\log_{10}(M_*\ [M_\odot])$	r_h ($r_{e,r}$)	N_{GC}	$\log_{10}(M_{halo}\ [M_\odot])$
FDS12_LSB50	−15.0	1.55	8.0	{0.80, 1.72, 2.70}	{0.4, 3.1, 9.6}	{9.2, 10.2, 10.7}
FDS12_LSB52	−12.1	0.51	6.2	{0.94, 1.81, 2.72}	{0.6, 3.1, 8.2}	{9.4, 10.2, 10.6}
FDS12_LSB53	−13.2	0.73	7.0	{0.76, 1.71, 2.73}	{0.3, 2.1, 6.3}	{9.1, 10.0, 10.5}
FDS12_LSB54	−12.4	0.46	6.6	{0.71, 1.74, 2.78}	{0.7, 3.4, 9.1}	{9.5, 10.2, 10.7}
FDS16_LSB6	−12.0	0.33	6.4	{0.56, 1.22, 2.19}	{0.7, 2.0, 4.2}	{9.4, 10.0, 10.3}
FDS16_LSB7	−14.7	1.38	7.8	{0.74, 1.67, 2.80}	{1.5, 6.5, 15.7}	{9.8, 10.5, 11.0}
FDS16_LSB10	−11.9	0.40	6.5	{0.68, 1.65, 2.61}	{0.1, 0.8, 2.4}	{8.6, 9.5, 10.0}
FDS16_LSB11	−14.4	1.16	7.7	{0.81, 1.61, 2.59}	{1.1, 5.0, 12.3}	{9.7, 10.4, 10.8}
FDS16_LSB12	−10.3	0.36	5.8	{0.84, 1.77, 2.75}	{0.2, 1.4, 3.9}	{8.9, 9.8, 10.3}
FDS16_LSB14	−10.1	0.46	5.9	{0.91, 1.81, 2.78}	{0.3, 1.8, 4.7}	{9.0, 9.9, 10.4}
FDS16_LSB16	−9.9	0.33	5.5	{0.65, 1.58, 2.63}	{0.1, 0.8, 2.3}	{8.6, 9.5, 10.0}
FDS16_LSB20	−14.4	1.26	7.6	{0.83, 1.92, 2.88}	{2.4, 8.7, 18.7}	{10.1, 10.7, 11.0}
FDS16_LSB24	−11.0	0.40	6.1	{0.71, 1.64, 2.66}	{0.3, 1.6, 5.1}	{9.0, 9.9, 10.4}
FDS16_LSB25	−15.1	1.39	8.0	{1.12, 1.74, 2.42}	{12.4, 22.5, 36.1}	{10.8, 11.1, 11.4}
FDS16_LSB26	−9.9	0.34	5.8	{0.72, 1.70, 2.68}	{0.1, 0.8, 2.5}	{8.6, 9.5, 10.1}
FDS16_LSB28	−11.9	0.49	6.6	{0.67, 1.67, 2.72}	{0.2, 1.5, 4.7}	{8.9, 9.8, 10.4}
FDS16_LSB30	−10.4	0.40	5.9	{0.80, 1.73, 2.72}	{0.2, 1.2, 3.4}	{8.8, 9.7, 10.2}
FDS16_LSB31	−11.4	0.85	6.4	{1.18, 1.96, 2.83}	{1.2, 4.5, 9.9}	{9.7, 10.4, 10.7}
FDS16_LSB32	−12.5	0.63	6.8	{0.66, 1.53, 2.55}	{0.7, 2.8, 6.7}	{9.4, 10.1, 10.5}
FDS16_LSB33	−12.2	0.55	6.7	{0.25, 0.91, 2.02}	{0.5, 1.8, 4.2}	{9.3, 9.9, 10.3}
FDS16_LSB34	−12.7	0.95	6.9	{0.82, 1.76, 2.71}	{0.6, 3.0, 8.9}	{9.3, 10.2, 10.7}
FDS16_LSB35	−11.6	0.47	6.5	{1.13, 1.97, 2.83}	{0.8, 3.3, 6.6}	{9.5, 10.2, 10.5}
FDS16_LSB36	−13.2	0.88	7.1	{0.76, 1.65, 2.63}	{0.5, 2.7, 7.6}	{9.3, 10.1, 10.6}
FDS16_LSB37	−12.6	0.52	6.8	{0.40, 1.35, 2.42}	{0.8, 3.1, 8.1}	{9.5, 10.2, 10.6}
FDS16_LSB38	−13.2	0.88	7.0	{1.12, 2.12, 3.04}	{0.7, 4.2, 12.7}	{9.4, 10.3, 10.9}
FDS16_LSB39	−10.8	0.71	5.9	{0.54, 1.38, 2.44}	{0.7, 2.8, 6.6}	{9.4, 10.1, 10.5}
FDS16_LSB40	−10.2	0.47	6.3	{1.02, 1.78, 2.69}	{1.3, 4.5, 9.7}	{9.8, 10.4, 10.7}
FDS16_LSB41	−11.4	0.49	6.4	{0.67, 1.66, 2.59}	{0.1, 0.9, 2.9}	{8.7, 9.5, 10.1}
FDS16_LSB42	−12.2	0.70	6.8	{0.79, 1.77, 2.78}	{0.3, 1.8, 5.6}	{9.0, 9.9, 10.5}
FDS16_LSB43	−14.4	1.17	7.6	{0.58, 1.54, 2.61}	{1.9, 6.5, 14.0}	{9.9, 10.5, 10.9}
FDS16_LSB44	−10.0	0.67	5.1	{0.82, 1.67, 2.64}	{0.3, 2.0, 5.9}	{9.1, 10.0, 10.5}
FDS16_LSB45	−13.6	1.79	7.4	{1.04, 1.83, 2.70}	{5.0, 14.0, 26.4}	{10.4, 10.9, 11.2}
FDS16_LSB47	−11.3	0.85	6.2	{1.00, 1.86, 2.79}	{0.6, 3.3, 8.3}	{9.4, 10.2, 10.7}
FDS16_LSB49	−11.5	0.81	5.9	{0.89, 1.80, 2.80}	{0.4, 2.5, 7.6}	{9.2, 10.1, 10.6}
FDS16_LSB50	−13.1	0.96	7.0	{0.93, 1.90, 2.83}	{0.3, 2.1, 6.3}	{9.0, 10.0, 10.5}
FDS16_LSB52	−10.3	0.72	6.0	{0.64, 1.60, 2.68}	{0.2, 1.0, 3.0}	{8.8, 9.6, 10.2}
FDS16_LSB54	−11.2	0.66	5.7	{0.70, 1.55, 2.53}	{0.2, 1.4, 4.0}	{8.9, 9.8, 10.3}
FDS16_LSB55	−12.3	0.81	6.8	{0.73, 1.57, 2.62}	{0.5, 2.7, 7.8}	{9.3, 10.1, 10.6}
FDS16_LSB56	−10.4	0.31	11.6	{0.58, 1.57, 2.60}	{0.1, 0.7, 2.0}	{8.5, 9.4, 10.0}
FDS16_LSB58	−15.1	1.70	8.0	{0.79, 1.56, 2.59}	{1.0, 4.5, 11.4}	{9.6, 10.3, 10.8}
FDS16_LSB59	−10.9	0.35	6.3	{0.75, 1.68, 2.67}	{0.2, 1.2, 3.1}	{8.9, 9.7, 10.2}
FDS16_LSB60	−11.6	1.02	6.6	{0.27, 1.33, 2.44}	{1.2, 3.8, 8.8}	{9.7, 10.3, 10.7}
FDS16_LSB63	−11.9	0.64	6.7	{0.72, 1.73, 2.67}	{0.1, 1.0, 3.4}	{8.7, 9.6, 10.2}
FDS16_LSB64	−12.3	1.04	6.6	{0.96, 1.81, 2.75}	{0.5, 3.2, 9.9}	{9.3, 10.2, 10.7}
FDS16_LSB65	−10.3	0.62	7.6	{0.83, 1.69, 2.68}	{0.3, 1.6, 4.5}	{9.0, 9.8, 10.3}
FDS16_LSB66	−11.0	1.04	6.8	{0.87, 1.75, 2.72}	{0.5, 2.5, 7.0}	{9.2, 10.1, 10.6}
FDS16_LSB67	−10.2	0.46	5.5	{0.68, 1.63, 2.66}	{0.2, 0.9, 2.9}	{8.7, 9.6, 10.1}
FDS16_LSB70	−11.7	0.86	6.3	{0.14, 1.20, 2.42}	{0.9, 3.4, 9.0}	{9.6, 10.2, 10.7}
FDS16_LSB71	−12.7	0.64	6.9	{0.13, 1.34, 2.75}	{1.2, 4.0, 11.4}	{9.7, 10.3, 10.8}
FDS16_LSB72	−12.0	0.58	6.7	{1.04, 2.01, 2.98}	{0.4, 2.6, 7.5}	{9.2, 10.1, 10.6}
FDS16_LSB74	−12.4	0.87	6.9	{0.77, 1.73, 2.79}	{0.3, 1.8, 5.6}	{9.0, 9.9, 10.5}
FDS16_LSB75	−10.8	0.53	5.8	{0.98, 1.87, 2.85}	{1.3, 4.5, 9.7}	{9.7, 10.3, 10.7}
FDS16_LSB77	−12.1	0.73	6.6	{0.65, 1.65, 2.69}	{0.2, 1.2, 4.1}	{8.8, 9.7, 10.3}
FDS16_LSB78	−10.8	0.37	6.1	{0.67, 1.73, 2.77}	{0.2, 1.1, 3.4}	{8.8, 9.7, 10.2}
FDS16_LSB79	−12.6	0.88	7.1	{0.76, 1.72, 2.73}	{0.2, 1.5, 4.9}	{8.9, 9.8, 10.4}
FDS16_LSB83	−12.5	0.76	6.7	{0.90, 1.79, 2.79}	{0.8, 3.7, 9.0}	{9.5, 10.3, 10.7}
FDS16_LSB84	−11.5	0.67	6.8	{0.72, 1.57, 2.60}	{0.5, 3.2, 8.9}	{9.3, 10.2, 10.7}
FDS16_LSB85	−15.7	4.23	8.1	{0.63, 1.66, 2.70}	{0.7, 4.3, 12.5}	{9.5, 10.3, 10.8}
FDS16_LSB87	−12.6	0.52	6.7	{0.88, 1.85, 2.88}	{0.3, 2.0, 6.1}	{9.0, 10.0, 10.5}
FDS11_LSB2	−15.4	9.51	9.0	{1.25, 2.21, 3.22}	{3.3, 21.1, 66.8}	{10.2, 11.1, 11.7}
FDS10_LSB27	−14.7	1.45	7.8	{0.85, 1.78, 2.78}	{0.5, 3.0, 9.4}	{9.3, 10.2, 10.7}

This paper has been typeset from a TEX/LATEX file prepared by the author.